JOURNAL OF PETROLOGY | VOLUME 51 | NUMBER 12 | PAGES 2547–2570 | 2010 | doi:10.1093/petrology/egq073

Distribution of Mantle and Atmospheric Argon in Mantle Xenoliths from the Western Arabian Peninsula: Constraints on Timing and Composition of Metasomatizing Agents in the Lithospheric Mantle

A. I. BUIKIN[1,2], M. TRIELOFF[1]*, E. V. KOROCHANTSEVA[1,2], J. HOPP[1], M. KALIWODA[3], H.-P. MEYER[1] AND R. ALTHERR[1]

[1]INSTITUT FÜR GEOWISSENSCHAFTEN DER UNIVERSITÄT HEIDELBERG, IM NEUENHEIMER FELD 234–236, D-69120 HEIDELBERG, GERMANY

[2]VERNADSKY INSTITUTE FOR GEOCHEMISTRY, KOSYGIN ST. 19, 119991 MOSCOW, RUSSIA

[3]MINERALOGICAL STATE COLLECTION, LMU, THERESIENSTRASSE 41, D-80333 MÜNCHEN, GERMANY

RECEIVED OCTOBER 15, 2009; ACCEPTED OCTOBER 22, 2010

To investigate the geochemical behaviour of argon isotopes during mantle metasomatism and to obtain chronological information on the age of metasomatic events under the Arabian Shield, we analyzed mantle xenoliths and hornblende megacrysts from Saudi Arabian volcanic fields (Uwayrid, Al Birk) applying the ^{40}Ar–^{39}Ar dating technique. Two hornblende megacrysts yield plateau ages indicating formation or total resetting of the K/Ar system 1–2 Myr ago. The ultramafic xenoliths trapped mantle-derived and atmospheric argon in different proportions, resulting in variable isotopic compositions: $^{40}Ar/^{36}Ar$ ratios range from 296 (i.e. atmospheric) to ~10 500, reflecting interactions with isotopically and genetically different fluids and/or melts during recent mantle metasomatism. One such episode of metasomatism led to the formation of Ba-rich phlogopite, which yielded a saddle-shaped age spectrum with a maximum age estimate of ~18 Ma. Another episode, inducing formation of secondary pargasite in the lithospheric mantle, was dated to ~4 Ma. In the mantle xenoliths the concentration of mantle argon is clearly related to the intensity of metasomatism. Argon extraction by high-resolution stepwise heating allowed us to deconvolve various argon components distributed heterogeneously within single xenoliths and ascribe them to specific carrier phases. Pyroxenes generally preserve much higher $^{40}Ar/^{36}Ar$ ratios than olivine, as they contain up to 100 times higher concentrations of mantle argon, which also correlates with a higher fluid inclusion content in pyroxenes. Hydrous phases (phlogopite/amphibole) have more variable $^{40}Ar/^{36}Ar$ ratios. K and Cl concentrations and the argon isotope compositions of the Uwayrid xenoliths indicate distinct metasomatic agents, causing elemental and isotopic disequilibrium on a local scale. On the basis of correlations between Ar isotope composition and K and Cl concentration in the samples most strongly affected by the late metasomatic fluids, we suggest that metasomatic processes in the local mantle occurring simultaneously with the opening of the Red Sea were accompanied by the introduction of saline-water saturated fluids into deep lithospheric zones.

KEY WORDS: *argon; lithospheric mantle; mantle metasomatism; noble gases*

INTRODUCTION

Mantle-derived xenoliths transported to the Earth's surface by ascending magmas preserve textural, chemical and isotopic information about the physical and chemical evolution of their lithospheric source regions. In particular, the chemical and isotopic signatures of xenolith phases

*Corresponding author. Telephone: Int-49-6221-546022. Fax: Int-49-6221-544805. E-mail: mario.trieloff@geow.uni-heidelberg.de

(minerals, glass, fluid inclusions) may help to constrain the nature and age of metasomatizing events. To date, almost all studies on metasomatized xenoliths have been based on incompatible element abundances and on the signatures of Sr, Nd, Pb, O and Os isotopes. In this study, we use argon isotopes to constrain the age and nature of metasomatic events recorded in mantle xenoliths from two Cenozoic volcanic fields in the Arabian peninsula that are associated with the formation of the Red Sea.

Previous studies have shown that Red Sea rifting was preceded by intense volcanism in the Afar region leading to the formation of the Ethiopian flood basalt province, which is commonly ascribed to the impingement of a mantle plume head on the base of the lithosphere (e.g. Hofmann *et al.*, 1997; Baker *et al.*, 1998, 2002; Courtillot *et al.*, 1999; Pik *et al.*, 1999; Ukstins *et al.*, 2002; Coulié *et al.*, 2003). This hypothesis is sustained geochemically by the observation of high $^{3}He/^{4}He$ ratios up to 20 R_A (1 R_A = atmospheric ratio; $^{3}He/^{4}He = 1{\cdot}4 \times 10^{-6}$) (e.g. Marty *et al.*, 1996; Scarsi & Craig, 1996) as well as neon isotopic fingerprints in Zabargad peridotites and Arabian mantle xenoliths (Hopp *et al.*, 2004); values of $^{20}Ne/^{22}Ne$ range up to $12{\cdot}06 \pm 0{\cdot}22$, and calculated mixing lines in the neon three-isotope diagram are slightly but significantly distinct from the mid-ocean ridge basalt (MORB) line, indicating a small contribution of a primitive mantle plume component in neon. However, $^{3}He/^{4}He$ ratios in Arabian mantle xenoliths range between 6·2 and 8·1 R_A, not higher than the MORB range.

As one consequence of lithospheric break-up, the subcontinental mantle beneath the Saudi–Arabian rift shoulder was subjected to intense metasomatism, affecting mineral assemblages and also inducing cryptic metasomatic alteration that can be recognized in trace element patterns (Brueckner *et al.*, 1988; Henjes-Kunst *et al.*, 1990; Kurat *et al.*, 1993; Blusztajn *et al.*, 1995; Baker *et al.*, 1998, 2002) and also in the noble gases (Trieloff *et al.*, 1997; Hopp *et al.*, 2004, 2007).

The processes preceding the transportation of the mantle xenoliths to the surface can be divided into three major stages: (1) enrichment of clinopyroxene (Cpx) in incompatible elements and formation of Ba-rich phlogopite and intragranular Cr-pargasite [metasomatism 1 of Henjes-Kunst *et al.* (1990)]; (2) infiltration of melt and formation of secondary brown intergranular amphibole [metasomatism 2 of Henjes-Kunst *et al.* (1990)]; (3) interaction of the host magma with the xenoliths, magma devolatilization and entrapment of fluid inclusions within the xenoliths.

Noble gases are valuable tools to constrain the genesis and history of mantle-derived rocks, as various mantle reservoirs are characterized by different isotopic compositions (see also Hofmann, 1997). The deep mantle signature (Honda *et al.*, 1991; Trieloff *et al.*, 2000) is distinct from that of the shallow mantle as sampled through MORB (Moreira *et al.*, 1998) or the subcontinental lithospheric mantle (Dunai & Baur, 1995; Hopp *et al.*, 2004; Buikin *et al.*, 2005*a*). Mantle-derived rocks are characterized by solar-type helium and neon (Ozima & Podosek, 2002; Trieloff & Kunz, 2005) with $^{20}Ne/^{22}Ne$ ratios up to 12·5, higher than the atmospheric value of 9·8. As a result of massive mantle degassing in Earth's early history (e.g. Allègre *et al.*, 1986), primordial noble gas isotopes (e.g. ^{36}Ar, ^{130}Xe) are severely depleted in mantle-derived rocks, resulting in an excess of radiogenic isotopes (e.g. ^{40}Ar from ^{40}K decay, ^{129}Xe from ^{129}I decay) relative to the atmospheric composition. For example, the $^{40}Ar/^{36}Ar$ ratio in the mantle is much higher than the atmospheric value of 296: the shallow MORB mantle is characterized by high $^{40}Ar/^{36}Ar$ ratios (>28 000), whereas mantle plume sources display somewhat lower $^{40}Ar/^{36}Ar$ ratios; for example, 8000 for the Hawaiian mantle source (Trieloff *et al.*, 2003).

In contrast to mantle-derived fluids, old and deep crustal fluids are characterized by much lower $^{3}He/^{4}He$ ratios (<1 R_A), much more nucleogenic neon (i.e. rich in ^{21}Ne), and moderately radiogenic argon (e.g. Ozima & Podosek, 2002). As shown by previous studies (e.g. Hopp, 2002; Hopp *et al.*, 2004, 2007), the noble gases in Arabian mantle xenoliths are of mantle, not of crustal origin. Nevertheless, a young and shallow crustal component may be included in the frequently observed atmosphere-like component.

Argon in mantle-derived samples is usually a complex mixture of contributions of shallow (and possibly deep) mantle components and argon derived from the terrestrial atmosphere. The atmospheric component can be either indigeneous to the fluid that interacted with the rock (possibly because it was influenced by meteoric water or seawater), or could be due to direct incorporation of air (Ballentine & Barfod, 2000). Depending on their origin, these components can be trapped in a variety of phases of the respective rocks. For example, in basalt glasses, argon can be hosted by the glass matrix, vesicles, phenocrysts or alteration minerals, whereas in peridotitic rocks possible carriers are the major phases such as olivine, clino- and orthopyroxene, or minor hydrous phases or fluid inclusions. Separation of these endmembers is of crucial importance for the interpretation of different argon (and noble gas) sources or incorporation processes.

With this goal we determined the argon isotopic composition of neutron-irradiated mantle-derived rocks using the ^{40}Ar–^{39}Ar dating method, applying high-resolution stepwise heating. Apart from the detection of possible *in situ* radiogenic contributions, this method allows us to trace the degassing of major (here olivine, clino- and orthopyroxene, sometimes amphibole) and minor (e.g. phlogopite, amphibole, glass, secondary alteration, inclusions) phases via neutron-induced argon isotopes (^{39}Ar

from K, ^{37}Ar from Ca and ^{38}Ar from Cl). For example, degassing of pyroxene can be traced via ^{37}Ar from Ca, whereas amphibole can be traced via concomitant degassing of ^{39}Ar from K and ^{38}Ar from Cl. In this way, natural argon isotopes degassing simultaneously can be ascribed to these specific phases, and specific argon isotope ratios of single phases can be identified. Implicitly, clues to the origin of these phases are provided. Previous studies have shown that this approach is a useful tool to identify argon mantle endmembers (and their carrier phases); for example, in basalt glasses (Trieloff *et al.*, 2003), peridotitic rocks (Turner *et al.*, 1990; Trieloff *et al.*, 1997) or diamonds (Turner *et al.*, 1990; Johnson *et al.*, 2000).

To a certain degree, argon and volatile trace elements monitored by neutron-induced argon isotopes (Cl, K) can also be used to characterize the metasomatizing agents (Turner *et al.*, 1993), and thus help to constrain the complex interplay between metasomatic agents of different provenance and compositions.

GEOLOGICAL BACKGROUND

The Red Sea forms part of the Afro-Arabian rift system (Fig. 1), the largest active rift system on Earth. Rifting in the Red Sea area started in late Oligocene times and was preceded by flood basalt volcanism in Ethiopia and Yemen at 32–30 Ma (e.g. Baker *et al.*, 1996; Hofmann *et al.*, 1997; Courtillot *et al.*, 1999; Pik *et al.*, 1999; Ukstins *et al.*, 2002; Coulié *et al.*, 2003). Seafloor spreading in the Red Sea commenced relatively recently, about 5 Myr ago (Bohannon *et al.*, 1989). Apart from Afar, volcanism was almost exclusively confined to the Arabian side of the Red Sea; in Egypt and Sudan Cenozoic volcanism is sparse. The bulk of the volcanic rocks exposed on the Arabian peninsula were erupted during the last 10 Myr (Coleman *et al.*, 1983; Camp & Roobol, 1989, 1991, 1992). Xenoliths derived from the mantle and lower crust have been found in most of the volcanic fields and are especially abundant in Quaternary mafic volcanic rocks (e.g. Kuo & Essene, 1986; McGuire, 1987, 1988; Henjes-Kunst *et al.*, 1990; McGuire & Stern, 1993; Blusztajn *et al.*, 1995; Baker *et al.*, 1998, 2002; Al-Mishwat & Nasir, 2004).

Uplift and erosion have exposed the crystalline basement over a large area; this forms part of the Arabian–Nubian Shield. The central part of this shield consists of juvenile mantle-derived oceanic and intra-oceanic island-arc crust of late Precambrian (Pan-African) age. The western and eastern parts of the shield mainly consist of older continental rocks reworked during the Pan-African orogeny (Henjes-Kunst *et al.*, 1990, and references therein). The Uwayrid volcanic field is situated on the eastern flank of the Red Sea rift, in the northeastern part of the Arabian–Nubian Shield, whereas the Al Birk volcanic field is located within the southern part of the rift graben (Fig. 1).

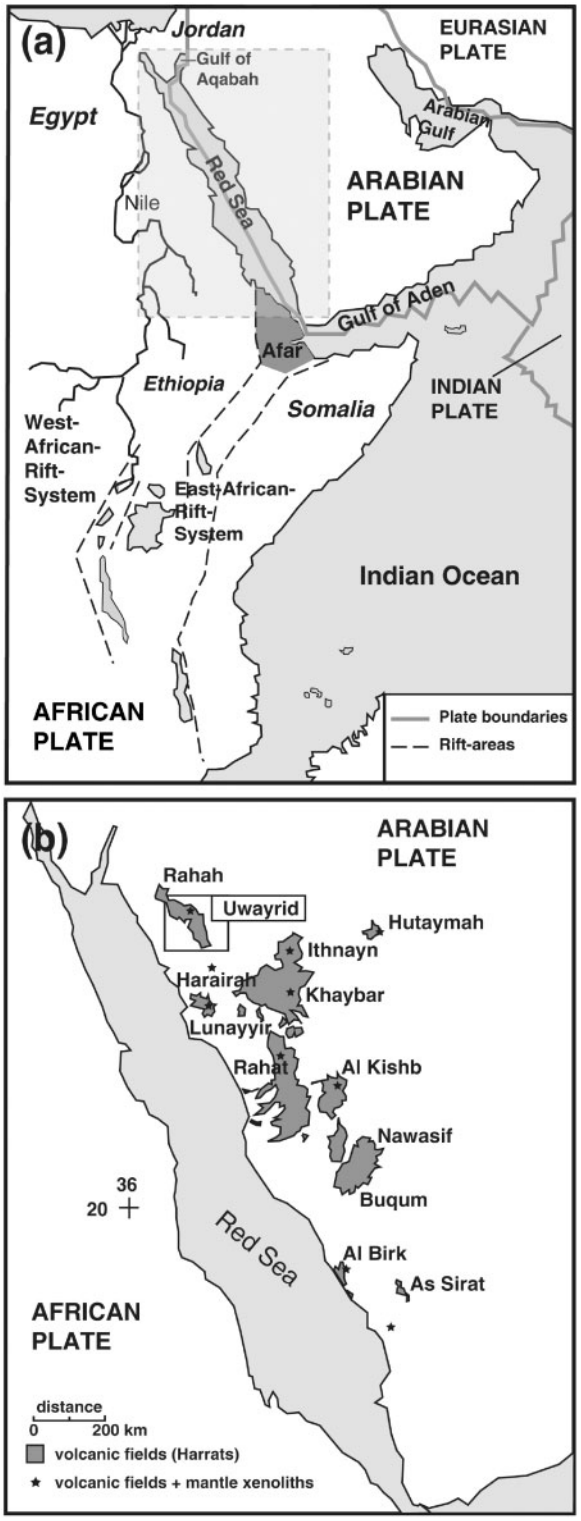

Fig. 1. Map showing the distribution of Saudi Arabian volcanic fields [reproduced from Kaliwoda *et al.* (2007)] and the xenolith localities.

EXPERIMENTAL METHODS

Polished thin sections of selected xenoliths were investigated in a previous study (Kaliwoda, 2004; Kaliwoda *et al.*, 2007). Scanning electron microscopy was used to investigate the presence of intergranular glass and fine-grained mineral phases. Major element compositions of minerals were determined using a Cameca SX51 electron microprobe equipped with five wavelength-dispersive spectrometers. Equilibration temperatures of the xenoliths were estimated by applying the two-pyroxene thermometer based on the enstatite–diopside solvus to the compositions of both pyroxene cores and rims [using the calibration of Brey & Köhler (1990*a*, *b*)]. Temperature-dependent pressures estimates were obtained from the Ca exchange between olivine and clinopyroxene (Köhler & Brey, 1990*a*, *b*).

For argon analyses performed in this study, coarse-grained (~50–200 μm) mineral separates were obtained by various steps of magnetic separation and hand-picking under a binocular microscope. ^{40}Ar–^{39}Ar analysis followed standard procedures given by Jessberger *et al.* (1980) and Trieloff *et al.* (1997, 2003). Whole-rock samples and mineral separates were wrapped in high-purity Al-foil and irradiated in an evacuated quartz ampoule. To minimize neutron-induced ^{36}Ar production by the $^{40}Ca(n,n\alpha)^{36}Ar$ reaction, irradiation at the GKSS reactor in Geesthacht, Germany, was limited to 1 day for the xenolith and 3 days for the megacryst samples, respectively. As previously (Trieloff *et al.*, 2003), we enhanced ^{38}Ar production from Cl by omitting the cadmium shielding, yielding significant contributions of thermal neutrons to the $^{37}Cl(n,\gamma\beta^-)^{38}Ar$ reaction. This allowed measurements of Cl concentrations down to 100 ppb with precisions down to ±5 ppb. For hornblende megacryst and xenolith samples, respectively, the $\mathcal{J}$-value was 9×10^{-4} and 3×10^{-4} as determined by NL25 hornblende flux monitors (Schaeffer & Schaeffer, 1977). The corresponding flux of fast neutrons was $0{\cdot}2 \times 10^{18}$ and $0{\cdot}07 \times 10^{18}$, and the total flux including thermal neutrons was $7{\cdot}4 \times 10^{18}$ and $2{\cdot}5 \times 10^{18}$, respectively. Typical neutron flux variations along irradiation capsules were 1–2%, and typical $\mathcal{J}$-value uncertainties of single samples monitored via NL25 standards were 0·2–0·4%. Correction factors for interfering isotopes determined by CaF_2 monitors were $(^{36}Ar/^{37}Ar)_{Ca} = (4{\cdot}6 \pm 0{\cdot}2) \times 10^{-4}$ and $(5{\cdot}0 \pm 1{\cdot}8) \times 10^{-4}$, $(^{38}Ar/^{37}Ar)_{Ca} = (11{\cdot}6 \pm 0{\cdot}2) \times 10^{-4}$ and $(8{\cdot}6 \pm 0{\cdot}5) \times 10^{-4}$, $(^{39}Ar/^{37}Ar)_{Ca} = (9{\cdot}8 \pm 0{\cdot}1) \times 10^{-4}$ and $(9{\cdot}3 \pm 0{\cdot}3) \times 10^{-4}$. $(^{38}Ar/^{39}Ar)_K = (2{\cdot}0 \pm 0{\cdot}5) \times 10^{-2}$ was taken as an average from previous Cd-shielded irradiations, $(^{40}Ar/^{37}Ar)_{Ca} = (3 \pm 3) \times 10^{-3}$ by Turner (1971) and $(^{40}Ar/^{39}Ar)_K = (1{\cdot}23 \pm 0{\cdot}24) \times 10^{-2}$ by Brereton (1970). The samples were stepwise heated to temperatures from 350°C to 1700°C (monitored by a thermocouple) using an induction-heated furnace with ^{40}Ar blank values of 0·01–0·02 at 1000°C and 0·05–0·10 at 1400°C ($\times 10^{-8}$ cm^3 STP, 10 min heating duration). Apparent ages were calculated using the Steiger & Jäger (1977) conventions (e.g. decay constants, K isotope ratio). Given uncertainties in apparent ages and isotope ratios are 1σ. Detailed argon isotope data tables are provided as electronic supplementary material.

SAMPLE DESCRIPTIONS: XENOLITH TEXTURES AND MINERAL COMPOSITIONS

Many xenoliths from the Harrat Uwayrid region contain secondary pargasite formed at the expense of clinopyroxene and spinel (Fig. 2a). In addition, many xenoliths are characterized by intergranular glass films or interstitial patches consisting of glass, phenocrysts (olivine, clinopyroxene, Cr–Al spinel) and former gas bubbles, suggesting that these rocks were infiltrated by melts prior to incorporation in ascending magmas (Henjes-Kunst *et al.*, 1990; Kaliwoda *et al.*, 2007). Textural relationships suggest that

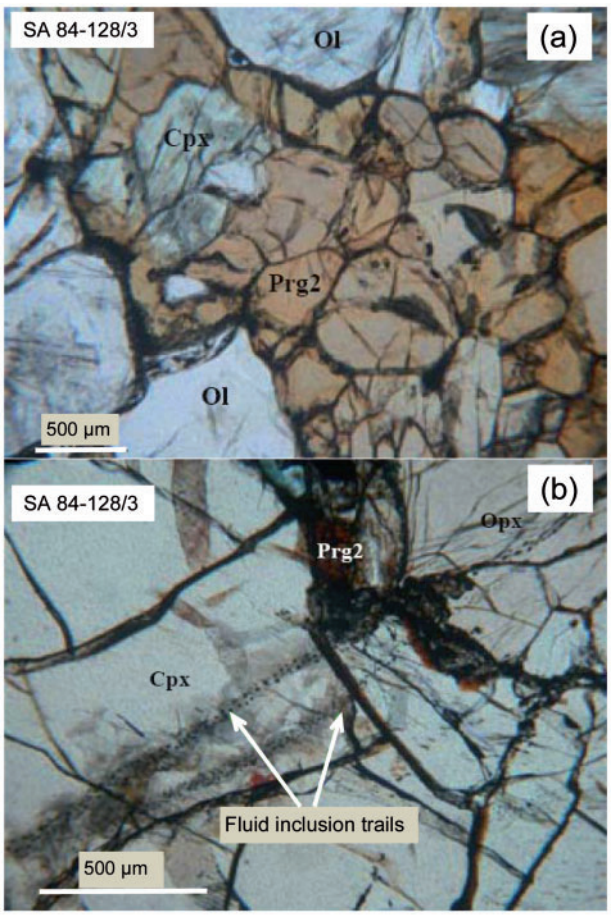

Fig. 2. (a) Secondary intergranular pargasite formed at the expense of clinopyroxene in SA84-128/3; (b) fluid inclusion trails crossing primary Cpx, Opx and secondary pargasite, formed during a late metasomatic event.

formation of secondary pargasite preceded the infiltration of melts that were quenched to glass. Some xenoliths with secondary pargasite are virtually free of glass and some xenoliths that contain glass do not contain pargasite. Furthermore, the glasses (including their phenocrysts) do not represent infiltrated host magmas and the melts did not form by breakdown of amphibole.

In the course of this study, we aimed at analyzing the effects of mantle metasomatism on the small-scale distribution of mantle and atmospheric argon in mantle xenoliths. We selected five xenoliths from Harrat Uwayrid and one (SA87-6/9) from Harrat Al Birk. These samples have been well characterized petrologically and mineralogically in previous studies, demonstrating that their protoliths were metasomatized to varying degrees, most probably by interaction with different agents (Henjes-Kunst *et al.*, 1990; Kaliwoda *et al.*, 2007). Two samples representing the more extreme metasomatic endmembers [called metasomatism 1 and metasomatism 2 by Henjes-Kunst *et al.* (1990); corresponding to samples SA84-63 and SA84-128/3, respectively] were studied here in more detail using mineral separates; other samples were used to document the absence of major metasomatism. All the samples are described below in more detail, and listed in Table 1 (including the most important petrological and metasomatic features) in order of decreasing degree of metasomatism.

SA84-128/3: pargasite-rich lherzolite

This xenolith has a heterogranular, weakly foliated texture (Kaliwoda *et al.*, 2007). Olivine has kink bands. Both pyroxenes contain abundant lamellae of complementary pyroxene and spinel. Two-pyroxene temperatures (Brey & Köhler, 1990*a*, *b*) are 987 ± 26 and 1028 ± 57°C (2σ) for core and rim compositions, respectively (at an assumed pressure of 1·5 GPa). At these temperatures, the Ca-in-olivine barometer yields $1{\cdot}75 \pm 0{\cdot}57$ and $2{\cdot}07 \pm 0{\cdot}57$ GPa, for core and rim respectively. Clinopyroxene is to a large degree replaced by brownish pargasite (Fig. 2a). Some clinopyroxene grains are completely transformed, whereas in other grains, the replacement has started from the rim and/or from fractures and exsolution lamellae. A total pargasite content of ~15 vol. % is estimated. Some glass is present within the interstices. In addition, minute amounts of secondary apatite and calcite occur in these areas. No relicts of spinel have been found. Fluid inclusion trails occur in all minerals and are most abundant in clinopyroxene and pargasite (Fig. 2b). Compared with the other xenoliths, SA84-128/3 contains significantly more fluid inclusions than SA84-38, SA84-123 and SA84-85.

SA84-63: spinel–pargasite–phlogopite–olivine websterite

This distinctive xenolith has a coarse-grained texture and is characterized by Cr-rich spinel [$X_{Cr} = Cr/(Cr + Al) \approx 0{\cdot}72$] and minor amounts of Ba-rich pargasite (~0·8 wt % BaO) included in clinopyroxene, as well as Ba-phlogopite (10–11 wt % BaO) and Sr-rich barite. All the Ba-rich minerals are in textural equilibrium with clinopyroxene, olivine, orthopyroxene and spinel. Both pyroxenes contain exsolution lamellae. Clinopyroxene grains are zoned with core-to-rim increases of Al and a decrease of Ca. Orthopyroxene grains are homogeneous in Ca and have core-to-rim decreases of Al. Two-pyroxene temperatures (Brey & Köhler, 1990*a*, *b*) are 900 ± 31 and 981 ± 37°C (2σ) for core and rim compositions, respectively. It has been suggested (Henjes-Kunst *et al.*, 1990; Kaliwoda *et al.*, 2007) that this xenolith represents former depleted mantle that was subject to metasomatic re-enrichment and subsequent recrystallization. Prior to incorporation into the ascending magma, an infiltrating melt phase reacted with the Ba-phlogopite, resulting in local formation of celsian (Ba-rich feldspar; 30–32 wt % BaO), Ba-rich glass (4·5–4·8 wt % BaO) and secondary spinel as well as olivine at the rim of phlogopite grains. Abundant fluid inclusion trails are present in both pyroxenes and in olivine.

SA87-6/9: spinel lherzolite

This virtually anhydrous xenolith (from Harrat Al Birk) is coarse-grained and weakly foliated. Pyroxenes do not have exsolution lamellae, but contain abundant fluid inclusions. An intergranular fluid has reacted with pyroxenes and olivine resulting in recrystallization of fine-grained pyroxene and olivine. Spinel is only locally corroded. In thin section, no glass has been identified.

SA84-38: spinel lherzolite

The texture of this xenolith is similar to that of sample SA84-85 (Kaliwoda *et al.*, 2007). Both pyroxenes contain exsolution lamellae and are weakly zoned with core-to-rim decreases of Al and an increase of Ca in clinopyroxene, suggesting slow cooling. At an assumed pressure of 1·5 GPa, two-pyroxene temperatures (Brey & Köhler, 1990*a*, *b*) are 874 ± 37 and 852 ± 82°C (2σ) for core and rim compositions, respectively. For a temperature of 860°C, the Ca-in-olivine barometer of Köhler & Brey (1990) yields $1{\cdot}72 \pm 0{\cdot}36$ GPa (2σ). Fluid inclusions are almost absent, whereas intergranular glass is abundant. Along interstices, larger glass patches contain tiny idiomorphic phenocrysts of olivine, clinopyroxene and spinel. At the contact with glass, primary spinel sometimes shows indented outlines as a result of corrosion. Minute amounts of secondary pargasite are present.

SA84-85: spinel lherzolite

According to Kaliwoda *et al.* (2007), this xenolith has a coarse-grained, weakly foliated texture. Olivine exhibits kink bands. Clinopyroxene contains rare thin exsolution lamellae of orthopyroxene, whereas orthopyroxene is free of lamellae. Both pyroxenes are only weakly zoned with minor core-to-rim decreases in Al. Application of the

Table 1: Metasomatic and petrological characteristics of the studied megacrysts and mantle xenoliths from the volcanic fields of Harrat Uwayrid and Harrat Al-Birk

Sample	Xenolith type	Hydrous minerals	Glass	Fluid inclusions	Two-pyroxene temperature core/rim (°C)	Weathering	Ar–Ar age (Ma)	$^{40}Ar/^{36}Ar$ (total)	$^{40}Ar/^{36}Ar$ (trapped, maximum)
SA84-64	Hornblende megacryst	Amphibole main constituent		? (too dark to recognize)		Not visible	~1·1	—	296
SA84-42B	Hornblende megacryst	Amphibole main constituent		? (too dark to recognize)		Not visible	~1·7	—	530 ± 40
SA84-128/3	Pargasite-rich lherzolite	15% brownish pargasite replacing cpx (metasomatism 2*)	Some interstitial glass	Abundant in all minerals	987 ± 26/1028 ± 57	Not visible	~4 (pargasite)	— 739 ± 16 (cpx)	330 ± 40 (pargasite) 2000 ± 500 (cpx)
SA84-63	Spinel-pargasite-phlogopite-olivine websterite	Ba-rich pargasite and phlogopite (metasomatism 1)		Abundant	900 ± 31/981 ± 37	Not visible	<18 (phlogopite)	3268 ± 63 (opx)	10500 ± 1200 (opx)
SA87-6/9	Spinel lherzolite	Anhydrous	No glass	Abundant in pyroxene		Not visible	—	3096 ± 142	4400 ± 100
SA84-38	Spinel lherzolite	Rare secondary pargasite (metasomatism 2)	Intergranular glass abundant	Almost absent	874 ± 37/852 ± 82	Not visible	—	1094 ± 132	2800 ± 500
SA84-85	Spinel lherzolite	Anhydrous	No glass	Rare	875 ± 65	Not visible	—	643 ± 33	3000 ± 1000
SA84-123	Spinel lherzolite	Rare tiny pargasite grains (metasomatism 2)	No glass	Almost absent	805 ± 68/844 ± 73	Thin films of brownish alteration	—	492 ± 41	1700 ± 800

*SA84-128/3 also experienced metasomatism 1 but was heavily overprinted by metasomatism 2.
The samples are listed in order of decreasing intensity of metasomatism. Henjes-Kunst *et al.* (1990) identified two types of relatively late metasomatism: metasomatism 1 inducing, for example, intergranular Ba-phlogopite, and a later metasomatism 2 inducing intergranular amphibole and melt patches. Whereas earlier metasomatism 1 is accompanied by argon with high $^{40}Ar/^{36}Ar$ ratios, later metasomatism 2 has argon with rather low $^{40}Ar/^{36}Ar$ ratios.

two-pyroxene thermometer of Brey & Köhler (1990*a*, *b*) in combination with the Ca-in-olivine barometer of Köhler & Brey (1990) yielded 875 ± 65°C (2σ) and $1{\cdot}28 \pm 0{\cdot}36$ GPa (2σ) for both core and rim compositions (Kaliwoda *et al.*, 2007). Rare fluid inclusion trails are present in olivine, clinopyroxene and, more rarely, also in orthopyroxene. Locally, a fluid phase has reacted with spinel, clinopyroxene and orthopyroxene, resulting in a weakly corroded, scarred surface of spinel grains and fluid inclusion-rich outer zones of pyroxene grains. The rock is virtually anhydrous (no pargasite or phlogopite) and free of glass.

SA84-123: spinel lherzolite

The texture of this xenolith is heterogranular and weakly foliated (Kaliwoda *et al.*, 2007). Both pyroxenes contain thin exsolution lamellae and show core-to-rim decreases of Al and an increase of Ca in clinopyroxene, suggesting cooling. Two-pyroxene temperatures are 805 ± 68 and 844 ± 73°C (2σ; at 1·5 GPa) for core and rim compositions, respectively. A maximum pressure value of $1{\cdot}54 \pm 0{\cdot}01$ GPa was calculated using the barometer of Webb & Wood (1986). Very rare tiny grains of pargasite appear texturally equilibrated with the primary minerals. No glass was found. Spinel is weakly corroded as a result of reaction with a fluid phase (compare SA84-85). Along cracks and grain boundaries of olivine, thin films of brownish alteration products (smectite?) are visible.

Hornblende megacrysts

We also analysed two several centimetre-sized hornblende megacrysts from Harrat Uwayrid. SA84-64 is a kaersutite megacryst that is homogeneous in composition. SA84-42B is a hornblende megacryst and is pargasitic to kaersutitic in composition. It contains a few small inclusions of glass, olivine and spinel. Al and Na decrease from core to rim and Ca increases from core to rim; other elements are homogeneous. For further petrographic details, we refer to Kaliwoda (2004) and Kaliwoda *et al.* (2007).

RESULTS AND DISCUSSION

Below we discuss the isotopic composition of argon extracted by high-resolution stepwise heating from whole-rock samples and mineral separates of selected xenoliths from Harrat Uwayrid and Harrat Al Birk that are metasomatized to varying degrees. We follow the view of previous researchers that mantle metasomatism infiltrates xenoliths and their constituent phases with mantle noble gases to varying degrees. As investigated in previous studies, the bulk helium and neon inventory of the studied samples (SA84-63 and SA84-38: Hopp, 2002; SA87-6/9: Hopp *et al.*, 2004) points to the presence of mantle helium (between 6 and 8 R_A) and neon, with $^{20}Ne/^{22}Ne$ up to 11·2, and a slope significantly steeper than the MORB line in the neon three-isotope plot, similar to other peridotitic rocks from that region (Hopp *et al.*, 2004). A strongly radiogenic (i.e. old) crustal component was not detected.

Mixing of a ubiquitous atmospheric noble gas component with varying proportions of mantle noble gases results in local isotopic disequilibrium of, for example, argon and neon. This results in a heterogeneous small-scale distribution of mantle and atmospheric argon in mantle xenoliths. Isotopic disequilibrium of neon and argon and the concentration of argon in phases resulting from metasomatism are two strong arguments that indeed metasomatism and not inward diffusion determines the initial noble gas budget of peridotitic rocks (e.g. Trieloff *et al.*, 1997).

In this study, we use high-resolution stepwise argon extraction (particularly $^{40}Ar/^{36}Ar$ ratios) to study the microdistribution of mantle-derived and atmosphere-derived noble gas isotopes. Similar measurements for neon were not possible, as this would have required larger amounts of non-irradiated aliquots of these xeoliths, for which only limited material was available. However, our results are most probably valid for neon as well. The fundamental reasoning behind this is that argon isotopes residing in different mineral phases can be extracted separately because of different mineral retentivity (i.e. different diffusion characteristics). Previous studies (Trieloff *et al.*, 1997, 2003; Hopp & Trieloff, 2005) have identified degassing temperature ranges for typical laboratory schedules (i.e. for degassing times of about 15–60 min) and separate grain sizes of about a few hundred micrometres; for amphibole these are between 1050 and 1150°C, for pyroxenes between 1200 and 1450°C and for olivine between 1500 and 1650°C. Although we heated olivine until (nominally) 1680°C, there remains the possibility that some of the argon was not completely degassed, particularly when the high melting temperature of ~1700°C of Mg-rich mantle olivine (Mg-number of ~90) is considered. However, some test blanks taken immediately after the last sample extractions at >1700°C yielded mostly blank argon, in agreement with earlier reported studies (Hopp & Trieloff, 2005). Moreover, it should be taken into account that the degassing temperature is controlled by diffusion as long as argon isotopes reside in the lattice or in small fluid inclusions. Only large fluid inclusions (>100 μm) can decrepitate at lower temperature upon stepwise heating [e.g. Hopp & Trieloff (2005) observed variable decrepitation temperatures of olivine inclusions between 600 and 800°C), which should be kept in mind when analysing degassing spectra. Once a host phase is identified, further petrographic work studying metasomatism can elucidate the origin of this component. For example, detailed fluid inclusion studies (e.g. Török & De Vivo, 1995; Witt-Eickschen *et al.*, 2003) on mantle xenoliths have frequently shown that these are CO_2-rich, more abundant in pyroxene than in olivine, mostly occur along healed fractures (i.e. the majority are secondary) and record trapping depths within

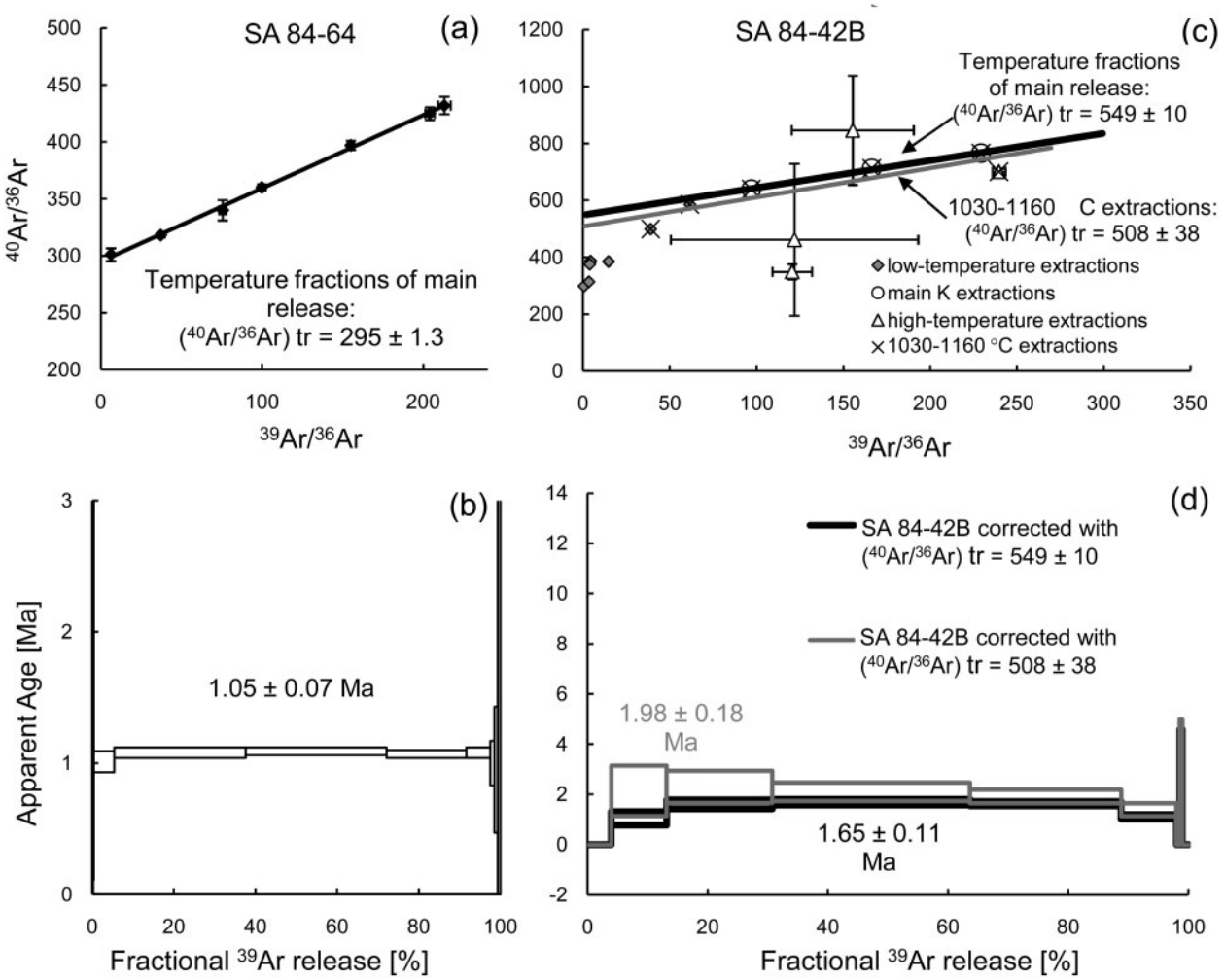

Fig. 3. Argon three-isotope plots and age spectra of hornblende megacrysts SA84-64 (a, b) and SA84-42B (c, d). The well-defined isochron in (a) indicates trapped argon of atmospheric composition. The age spectrum (b) forms a plateau over 97% of the ^{39}Ar release yielding an age of 1·05 ± 0·07 Ma. Correction of sample SA84-42B for a trapped argon component inferred from the partial isochron in (c) results in a plateau age of 1·65 ± 0·11 Ma if $(^{40}Ar/^{36}Ar)_{trapped} = 549 \pm 10$, or 1·98 ± 0·18 if $(^{40}Ar/^{36}Ar)_{trapped} = 508 \pm 38$.

the upper lithospheric mantle to lower- and mid-crustal levels. Variation of equilibration and trapping pressure was even observed between inclusions within single crystals or single inclusion trails and attributed to redistribution of the fluid content during fast uplift of the xenoliths (~10 m s^{-1}). Fluid influx from the rising and degassing magma was not excluded, but considered as minor. Hence, much of the trapped fluids can be expected to have an upper mantle signature. We also performed a prospective fluid inclusion study on thick sections of our xenolith samples and came to similar conclusions to those outlined above; for example, samples SA84-63 and SA84-128/3 display the expected CO_2-rich inclusions. Unfortunately, our amphibole sections were too dark or inclusions too small to be measured.

For non-zero age mantle rocks, the production of *in situ* radiogenic ^{40}Ar by ^{40}K decay has to be taken into account. In practice, however, only K-rich minerals such as amphibole or phlogopite contain significant amounts of *in situ* radiogenic ^{40}Ar. In such favourable cases gas retention ages may be calculated. In contrast, in K-poor minerals such as olivine and pyroxene, mantle ^{40}Ar is dominant, making apparent ages exceedingly high and chronologically meaningless (e.g. billions of years).

Hornblende megacrysts

Figure 3a displays a three-isotope plot of hornblende megacryst SA84-64. The data form a well-defined isochron, pointing to a simple two-component mixture of *in situ* radiogenic argon and a single trapped argon component

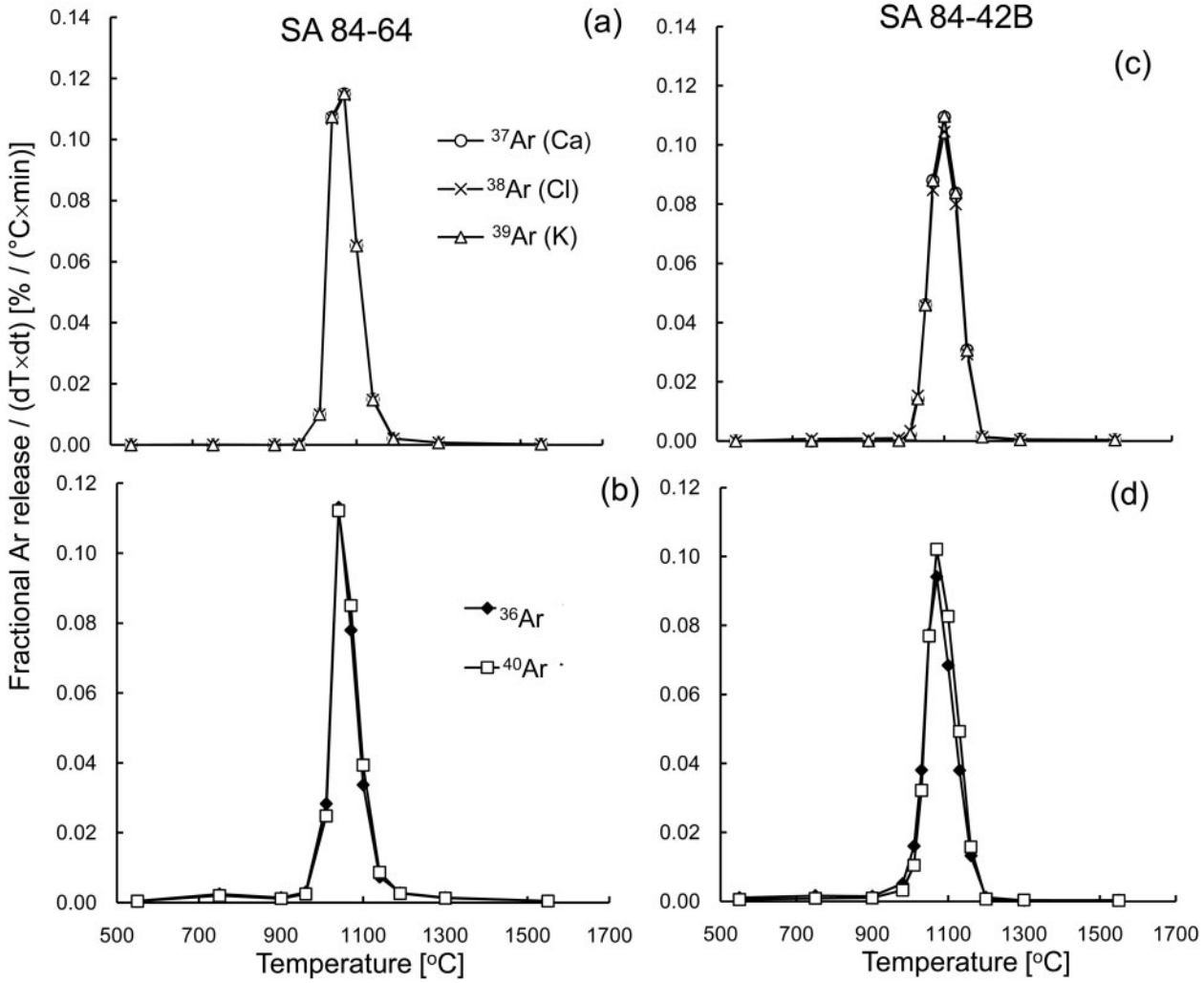

Fig. 4. Degassing pattern of argon isotopes in SA84-64 (a, b) and SA84-42B (c, d) samples. It should be noted that all spectra have sharp peaks around 1100°C, characteristic for amphiboles.

that has the isotopic composition of air (^{40}Ar/^{36}Ar = 296), as indicated by the *y*-axis intercept. The corresponding calculated age spectrum is shown in Fig. 3b: an age plateau over 97% of the ^{39}Ar release comprising five argon extractions yields an age of 1·05 ± 0·07 Ma.

For sample SA84-42B the presence of excess (probably mantle-derived) argon is indicated by the three-isotope plot (Fig. 3c), as most argon extractions tend to form an isochron pointing to a trapped argon component with ^{40}Ar/^{36}Ar >296: although some low-temperature extractions obviously have trapped argon with atmospheric composition, five extractions between 1030 and 1160°C form a line with $(^{40}Ar/^{36}Ar)_{trapped} = 508 \pm 38$, yielding a plateau age spectrum of 1·98 ± 0·18 Ma (grey line, Fig. 3d). The three temperature steps containing almost 80% of the ^{39}Ar define an isochron with $(^{40}Ar/^{36}Ar)_{trapped} = 549 \pm 10$; correction of the age spectrum with this value results in a plateau age of 1·65 ± 0·11 Ma (black line, Fig. 3d). However, these two age values are only marginally different at the 2σ level and consistent with an ~1·7 Ma age.

Figure 4 shows the release patterns of both natural (^{40}Ar, ^{36}Ar) and neutron-induced argon isotopes (^{39}Ar from K, ^{37}Ar from Ca, and ^{38}Ar from Cl). Both hornblende megacryst samples have sharp release peaks at ~1100°C for all isotopes. This degassing pattern is typical for hornblende (Trieloff *et al.*, 1997, and references therein) and indicates pure monomineralic samples. Using total contents of neutron-induced ^{39}Ar, ^{37}Ar and ^{38}Ar in the megacryst samples we calculated bulk concentrations of potassium, calcium and chlorine (Table 2). Within the corresponding uncertainties, which are about 5% for K and Ca contents, and up to 30% for Cl, these are in good agreement with data obtained from electron-microprobe analysis (EMPA) also reported in Table 2. This agreement

Table 2: Argon concentrations and isotopic compositions, and K, Cl, Ca concentrations and ratios in mantle xenoliths and their separates from the volcanic fields at Harrat Uwayrid and Harrat Al-Birk

	^{36}Ar (10^{-10} cm^3 g^{-1})	$^{40}Ar_{exc}$* (10^{-8} cm^3 g^{-1})	$^{40}Ar/^{36}Ar$	K† (ppm)	Cl† (ppm)	Ca† (%)	K/Cl	K/Ca (10^{-3})
SA84-64 hornblende megacryst	8·7 ± 0·1	0·05	361 ± 4	14600 ± 300 (13200 ± 300)	279 ± 7 (210 ± 80)	8·0 ± 0·2 (7·53 ± 0·09)	52 ± 1 (62 ± 25)	182 ± 5 (176 ± 5)
SA84-42B hornblende megacryst	9·1 ± 0·1	14·9	590 ± 10	15000 ± 400 (14000 ± 300)	277 ± 8 (286 ± 152)	8·0 ± 0·2 (7·44 ± 0·08)	54 ± 2 (49 ± 26)	188 ± 6 (188 ± 5)
SA84-128/3 WR‡	7·1 ± 0·3	7·9	408 ± 16	774 ± 9	111 ± 2	2·23 ± 0·02	7·0 ± 0·1	35 ± 1
Amph SA84-128/3	5·7 ± 0·2	3·9	364 ± 13	3300 ± 100 (3030 ± 200)	448 ± 16 (518 ± 130)	5·99 ± 0·22 (6·76 ± 0·30)	7·4 ± 0·4 (6·2 ± 1·6)	55 ± 3 (48 ± 4)
Cpx SA84-128/3§	8·6 ± 0·2	38·0	739 ± 16	354 ± 7 (64 ± 70)	50 ± 1	10·2 ± 0·2 (13·27 ± 0·08)	7·2	34·21 ± 0·01
Opx SA84-128/3§	5·1 ± 0·1	24·2	781 ± 12	127 ± 1 (2 ± 4)	17·8 ± 0·3	0·64 ± 0·02 (0·42 ± 0·04)	7·2	19·6 ± 0·1
Ol SA84-128/3	1·9 ± 0·1	1·3	363 ± 25	3 ± 0·2	0·33 ± 0·01	0·06 ± 0·01	7·8	3·9 ± 0·1
SA84-63 WR	12·6 ± 0·2	245·0	2246 ± 44	109 ± 7	13·6 ± 0·3	12·1 ± 1·7	8	0·90 ± 0·01
Cpx SA84-63	13·3 ± 0·3	291·6	2485 ± 81	95 ± 8 (90 ± 120)	21·0 ± 0·6	14·35 ± 0·54 (14·42 ± 0·4)	4·5	0·65 ± 0·01
Opx SA84-63§	6·3 ± 0·1	187·9	3268 ± 63	223 ± 3 (0 ± 0)	17·9 ± 0·4	0·56 ± 0·02 (0·42 ± 0·05)	12·6	39·6 ± 0·2
Ol SA84-63	1·7 ± 0·1	4·3	557 ± 33	2·6 ± 0·3	0·43 ± 0·02	0·015 ± 0·014	6	17·3 ± 0·7
Amph SA84-63 (intragranular in Cpx)				(4200 ± 200)		(6·87 ± 0·08)		(0·061 ± 0·03)
Phl SA84-63				(32700 ± 1500)	(1445 ± 256)	(0·11 ± 0·10)	(23 ± 3)	(30 ± 27)
SA87-6/9 WR	1·2 ± 0·1	33·1	3096 ± 142	5·6 ± 0·2	0·28 ± 0·01	1·86 ± 0·05	20	0·30 ± 0·01
SA84-38 WR	2·3 ± 0·3	18·6	1094 ± 132	12·0 ± 0·4	18·5 ± 0·7	0·65 ± 0·05	0·6	1·8 ± 0·1
SA84-85 WR	2·5 ± 0·1	8·7	643 ± 33	3·6 ± 1	0·10 ± 0·005	1·9 ± 0·05	35	0·19 ± 0·01
SA84-123 WR	2·1 ± 0·2	4·1	492 ± 41	23 ± 1	3·0 ± 0·1	2·06 ± 0·05	7	1·03 ± 0·1

†K, Ca, and Cl concentrations obtained by EMPA (given in parentheses) are average values, typically obtained from profiles across three mineral grains, each profile comprising between 150 and 300 points. Except for the Ca-zonation in pyroxene (see main text) no significant intra- or inter-grain variations were observed.
‡WR, whole rock.
*Excess ^{40}Ar calculated assuming all ^{40}Ar in excess of air is excess argon ($^{40}Ar_{exc} = {}^{40}Ar_{total} - 295{\cdot}5\ {}^{36}Ar$). For Hbl-megacrysts with high K contents and known age, *in situ* radiogenic argon was also taken into account ($^{40}Ar_{exc} = {}^{40}Ar_{total} - 295{\cdot}5\ {}^{36}Ar - {}^{40}Ar_{rad}$).
§For some pyroxene separates, the bulk K content inferred from ^{39}Ar is much higher than the K concentrations obtained by EMPA. The reason is that analyses by EMPA are spot analyses in thin section (and hence reflect the true K content of pyroxene), whereas the bulk analyses include K from impurities such as amphibole. Indeed, we used the excess K content to calculate the fraction of amphibole impurities in several pyroxene separates.

also confirms the absence of minor phases that could influence the K, Ca or Cl budget, and suggests no major systematic errors affecting the two methods. Bulk Ar concentrations, as well as $^{40}Ar/^{36}Ar$ and K/Cl and K/Ca ratios obtained from both argon analyses and EMPA, are also shown in Table 2.

Hornblende megacrysts SA84-64 and SA84-42B were erupted from cinder cones that are built on top of lava flows for which whole-rock K-Ar ages of 0·39 ± 0·02 Ma and 0·90 ± 0·05 Ma, respectively, have been obtained (H. Kreuzer & R. Altherr, unpublished data). The higher ages of the megacrysts imply that they formed before the host lava, either in the mantle or in a crustal magma chamber. Regarding the close to atmospheric signature of the trapped argon, the second scenario appears more probable. In any case, it is compelling that during the late

stages of magmatic evolution hydrous fluids present in the magmatic system were strongly influenced by an atmospheric component; for example, by interaction with meteoric water or seawater, possibly assimilated by the magma chamber. Similar conclusions were reached for late-stage amphiboles (so-called 'type III'—for definition see Agrinier *et al.*, 1993) within Zabargad peridotites (Trieloff *et al.*, 1997). We do not favour a simple incorporation of atmospheric argon (e.g. by surficial adsorption or incorporation by water–rock alteration, or after sample collection) because (1) the degassing temperature of the trapped argon component is similar to that for argon degassing from the amphibole lattice, and (2) the trapped component has an $^{40}Ar/^{36}Ar$ ratio significantly higher than air (i.e. must have equilibrated with a more radiogenic component).

Peridotite xenoliths

From two xenoliths characterized by significant modal metasomatic effects (pargasite lherzolite SA84-128/3 and spinel–pargasite–phlogopite olivine websterite SA84-63), one whole-rock fraction and various mineral fractions (amphibole, ortho- and clinopyroxene, olivine) were irradiated and investigated for their argon isotopic budgets. Figures 5–8 show argon isotope release patterns for two whole-rock fractions and separated minerals, and also $^{40}Ar/^{36}Ar$ ratios vs release temperature. We use, but also extend, results from previous work (Trieloff *et al.*, 1997) that evaluated mineral-specific release temperature intervals. For example, the degassing temperature range for amphibole is 1050–1150°C, for pyroxenes 1200–1450°C (clinopyroxene and orthopyroxene are hardly separable) and for olivine 1500–1650°C (Trieloff *et al.*, 1997, and references therein; Trieloff *et al.*, 2003; Hopp & Trieloff, 2005).

Pargasite lherzolite SA84-128/3

This xenolith is a former spinel lherzolite in which clinopyroxene and Cr–Al spinel have been replaced by secondary pargasite. A pargasite separate from this sample has a very similar argon release pattern (Fig. 5a and b) when compared with the hornblende megacryst samples, except for small, low-temperature peaks of the natural argon isotopes ^{40}Ar and ^{36}Ar. Similar to megacryst SA84-42B, the amphibole separate of this xenolith has a somewhat disturbed age spectrum pointing to the possible presence of excess ^{40}Ar. In an argon three-isotope diagram the data (excluding the 350°C fraction) form an isochron yielding a trapped argon component with $(^{40}Ar/^{36}Ar)_{trapped} = 305 \pm 20$; that is, hardly different from atmospheric composition (grey line, Fig. 5c). Correcting the age spectrum of the amphibole separate with this ratio yields a total integrated age of $2{\cdot}6 \pm 1{\cdot}2$ Ma (grey line, Fig. 5d). The integrated age of the SA84-128/3 whole-rock sample is significantly higher (~8–9 Ma). The whole-rock isochron displays more compelling hints for the presence of excess argon: SA84-128/3 whole-rock data form three clusters (black line, Fig. 5c); whereas the low-temperature extractions scatter towards the atmospheric argon composition, the extractions at intermediate temperatures (containing >90% of the K-derived argon released from amphibole) yield a correlation line with $(^{40}Ar/^{36}Ar)_{trapped} = 362 \pm 5$. An age spectrum corrected with this component yields a plateau over most of the ^{39}Ar release with an age of $3{\cdot}85 \pm 0{\cdot}40$ Ma (black line, Fig. 5d). Within the uncertainties, this is consistent with the integrated age of the amphibole separate, so we conclude that an age of ~4 Ma can serve as a rough age estimate for pargasite formation. It may be questioned why the amphibole separate and whole-rock amphibole component appear to have different trapped high $^{40}Ar/^{36}Ar$ values, although the difference is only marginal at the 2σ level. An additional explanation may be that the trapped component in the intermediate temperature extractions of the whole-rock sample, although amphibole dominated, is probably influenced by the tailing release peaks of the high $^{40}Ar/^{36}Ar$ phases (e.g. pyroxene and its inclusions) that overlap with the amphibole release regime.

Similar to the amphibole megacrysts, our chemical data (K, Ca, Cl concentrations) are in good agreement with the EMPA data (Table 2). The $^{40}Ar/^{36}Ar$ ratios of trapped argon in amphiboles of all three samples are relatively low, close to atmospheric composition, and suggest that all these amphiboles formed from fluids or melts that were significantly influenced by surface-related fluids, or had recently incorporated such fluids. The K/Cl ratios of intergranular pargasite (SA84-128/3) and the two megacrysts are different (~7 and ~50, respectively), but it is yet unclear whether this reflects a distinct composition of the metasomatic agents. It may simply be related to the different types of amphibole (Cr-pargasite in SA84-128/3 vs kaersutite megacrysts).

The argon release pattern of the SA84-128/3 orthopyroxene separate (Fig. 6b) shows two distinct peaks for neutron-induced isotopes. A high-temperature peak at 1300–1500°C is dominated by calcium-derived ^{37}Ar released from orthopyroxene (Trieloff *et al.*, 1997, and references therein), accompanied by minor release of potassium-derived ^{39}Ar and chlorine-derived ^{38}Ar. A second peak at intermediate temperatures (1100°C) is dominated by argon from K and Cl with a K/Cl ratio of 6·9. Both release temperature and K/Cl ratio agree well with the properties of intergranular amphibole from this sample. Obviously, our mineral separation techniques did not result in complete separation of amphibole from pyroxene. The presence of amphibole impurities in this separate also explains why the bulk K content of the pyroxene separate is significantly higher than measurements of K in pyroxene by EMPA (Table 2). From the K and Cl contents present in the amphibole peak of the orthopyroxene

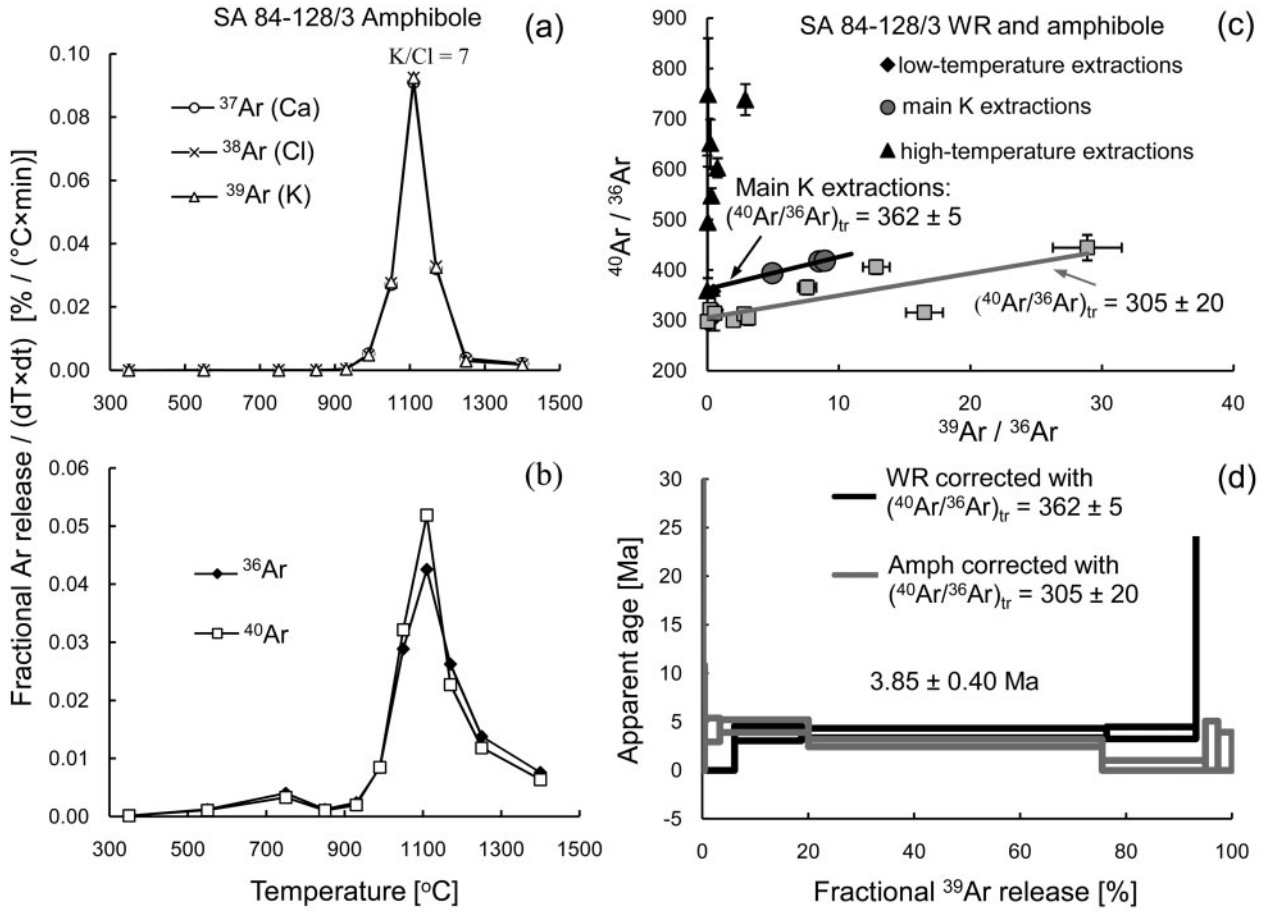

Fig. 5. (a, b) Degassing pattern of argon isotopes in SA84-128/3 amphibole. (c) Argon three-isotope plots for SA84-128/3 amphibole and whole-rock samples. Amphibole-separate data (excluding the 350°C fraction) form an 'isochron' yielding a relatively imprecise trapped argon component little different from the atmospheric composition. SA84-128/3 whole-rock data form three clusters: low-, high- and intermediate-temperature extractions. The last (containing >90% of the K-derived argon released from amphibole) yield a correlation line indicating $(^{40}Ar/^{36}Ar)_{trapped} = 362 \pm 5$. Correction of the whole-rock age spectrum with this value results in a plateau of 3·85 ± 0·40 Ma, consistent with the age of the amphibole separate (2·6 ± 1·2 Ma), as shown in (d).

separate we can calculate about 4% amphibole. SA84-128/3 clinopyroxene (Fig. 6a) also has two distinct release peaks, but the peaks are not very well resolved owing to the slightly lower degassing temperature of clinopyroxene when compared with orthopyroxene. From the K content of the clinopyroxene separate, an amphibole abundance of 10% can be calculated. It is important to note that the natural argon isotopes ^{36}Ar and ^{40}Ar are also released from these two phases in the pyroxene separates (middle panels in Fig. 6a and b), although with different isotopic compositions: high-temperature extractions dominated by pyroxene have significantly higher $^{40}Ar/^{36}Ar$ ratios, up to 2000, indicating the presence of significant amounts of mantle-derived argon (note that above we ruled out an old radiogenic crustal component based on the mantle type He and Ne inventory of Arabian mantle xenoliths; Hopp *et al.*, 2004). In addition, there are small low-temperature argon peaks with low $^{40}Ar/^{36}Ar$ ratios, most probably argon from less retentive minor alteration phases. This observation highlights the fact that even mineral separates can be complex mixtures exhibiting phase-specific, different isotopic compositions that point to different histories of formation and fluid trapping, with noble gases from different sources. As minor phases can significantly influence the argon budget, total fusion analyses yield meaningless average isotope ratios. Hence, stepwise heating is a powerful and mandatory tool to disentangle these different components.

The SA84-128/3 olivine separate has very low Ar and K, Ca and Cl concentrations (Table 2). The K and Cl contents of 3 and 0·33 ppm, respectively, suggest an upper limit of 0·1% for amphibole impurities. Moreover, a significant proportion of neutron-induced argon isotopes is released at relatively low temperatures (Fig. 6c), probably from alteration phases, and accompanied by natural argon with low $^{40}Ar/^{36}Ar$ ratios (lower panel in Fig. 6c). At high

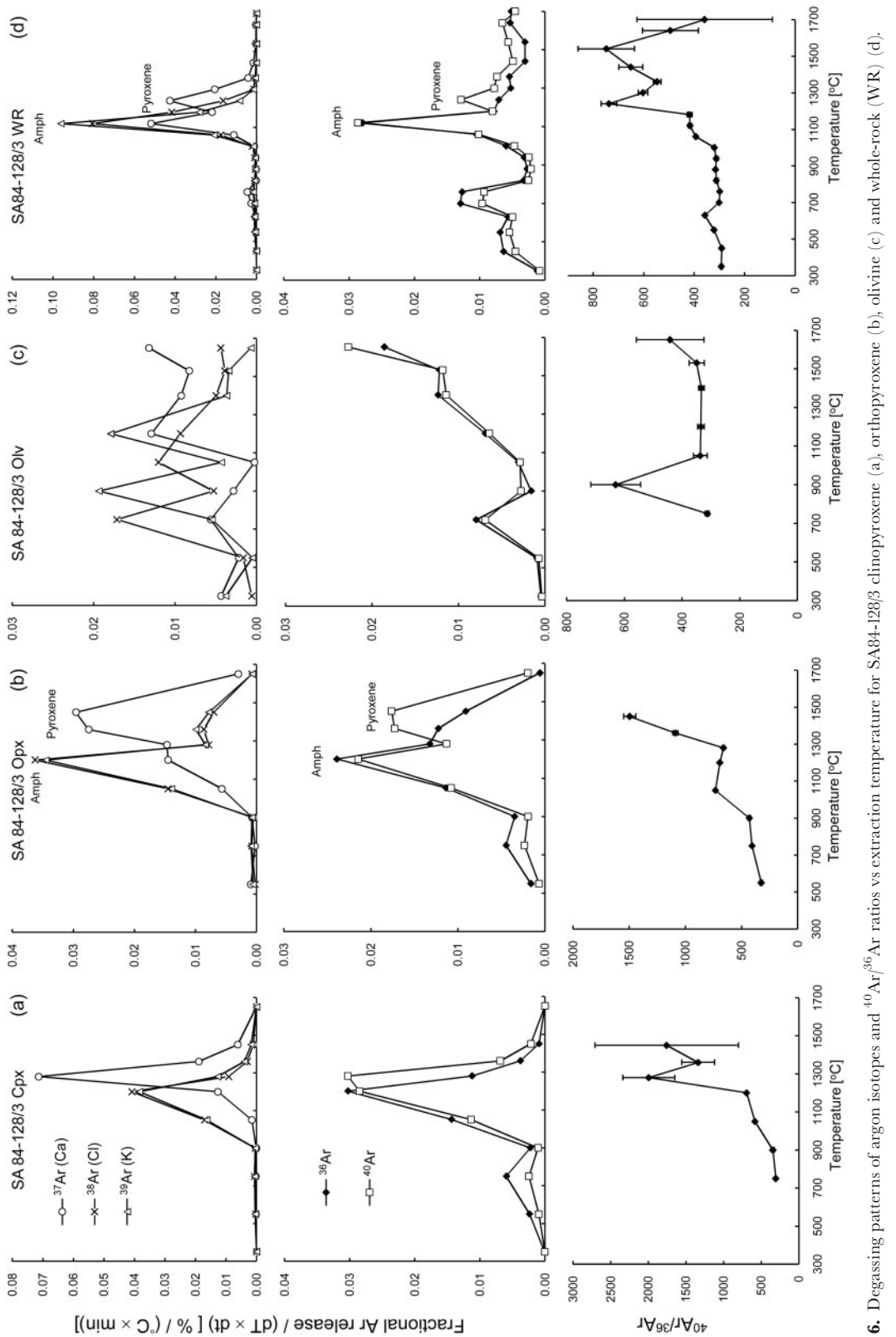

Fig. 6. Degassing patterns of argon isotopes and $^{40}Ar/^{36}Ar$ ratios vs extraction temperature for SA84-128/3 clinopyroxene (a), orthopyroxene (b), olivine (c) and whole-rock (WR) (d).

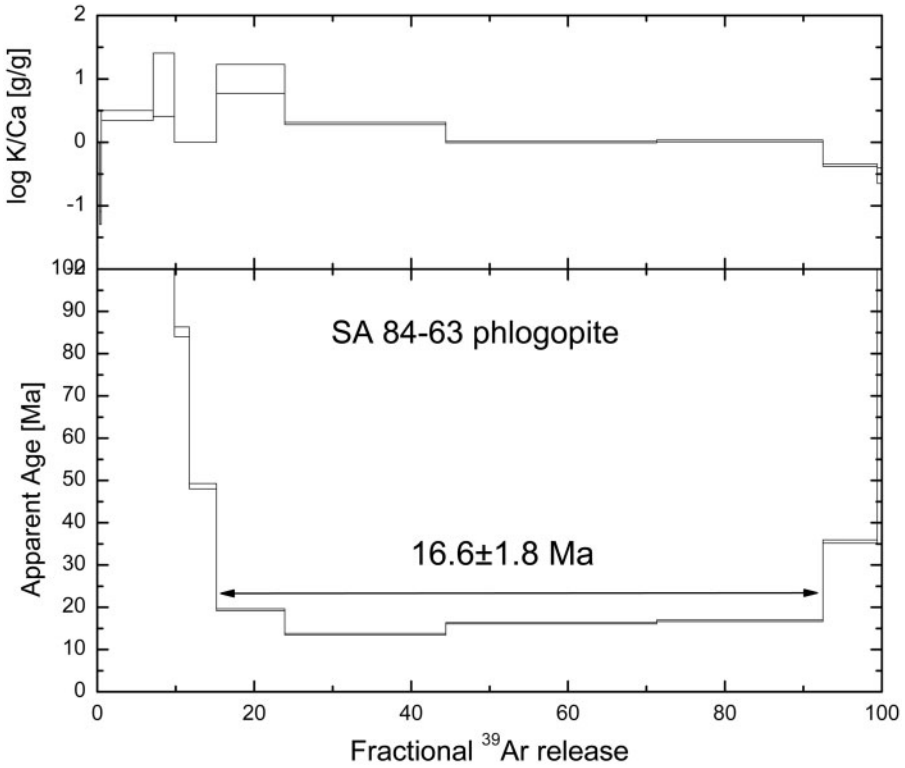

Fig. 7. Age spectrum of SA84-63 phlogopite. The saddle shape points to the presence of excess Ar. Four of the most gas-rich fractions (~75% of ^{39}Ar release) form a pseudo-plateau with an age of 16·6 ± 1·8 Ma, which should be considered as the upper age limit.

temperatures of >1500°C, the olivine degassing peak becomes apparent in ^{40}Ar and ^{36}Ar release, but the ^{40}Ar/^{36}Ar ratio appears only slightly higher (<560) than the atmospheric composition. Though cautioning that some argon may not have been completely extracted from the olivine at 1650°C, we preliminarily note that olivine from peridotites has a low affinity for trapping noble gases in general, particularly mantle-derived noble gases. Hence, mantle noble gas analyses should rather focus on pyroxene separates, to better eliminate atmospheric contaminants.

The argon release pattern of the whole-rock sample of SA84-128/3 (Fig. 6d) reflects the superimposition of all phases evaluated above. From the K, Ca, and Cl contents, we can calculate modal abundances of 20% amphibole, 65% olivine and 15% pyroxenes, assuming equal abundances of ortho- and clinopyroxene. This agrees with the modal abundances observed in thin section. However, the resolution of the argon release peaks is not satisfactory: they are partially superimposed upon each other; for example, amphibole and pyroxene, or pyroxene and olivine reservoirs. This is also reflected by the fact that no argon with ^{40}Ar/^{36}Ar > 1000 was observed at high temperatures.

There are also release peaks below 1000°C in the SA84-128/3 fractions, best recognizable for ^{40}Ar and ^{36}Ar. These could be related to secondary minerals such as smectite, calcite or zeolite (e.g. Poreda & Farley, 1992; Trieloff *et al.*, 1994, 1997). On the other hand, they could indicate the decrepitation of relatively large fluid inclusions. However, judging from the minor contributions of neutron-induced argon isotopes from K, Cl and Ca, and the atmosphere-like ^{40}Ar/^{36}Ar ratios, we favour secondary alteration phases as argon carriers.

Spinel–pargasite–phlogopite–olivine websterite SA84-63

This xenolith has generally higher concentrations of mantle argon, and correspondingly higher ^{40}Ar/^{36}Ar ratios in all phases. However, the argon distribution between phases has features very similar to pargasite lherzolite SA84-128/3.

A phlogopite separate from this xenolith shows a saddle-shaped age spectrum pointing to the presence of excess argon. However, four of the most gas-rich fractions (~75% of ^{39}Ar release) form a plateau-like structure defining an upper limit age of 16·6 ± 1·8 Ma (Fig. 7). This result is supported by Rb–Sr and Sm–Nd isotope data of Henjes-Kunst *et al.* (1990). This young age rejects our previous suggestion (Buikin *et al.*, 2005*b*) of a possible ancient age for the phlogopite formation, a reasoning that was based on whole-rock isochron analyses of this xenolith.

Similar to the SA84-128/3 pyroxene separates, the major release of Ca-derived ^{37}Ar occurs at high temperatures of 1200–1400°C from the main phase pyroxene, with clinopyroxene (Fig. 8a) having a slightly lower degassing temperature than orthopyroxene (Fig. 8b). The intermediate-temperature fractions are dominated by additional release of potassium- and chlorine-derived argon. Petrographic observations of this xenolith indicate that the dominant hydrous phase is phlogopite rather than amphibole or glass. With an EMPA-derived K content of 3·3% in phlogopite (Table 2), we can calculate maximum phlogopite contents of 0·3 wt %, 0·7 wt % and 0·3 wt % from the abundances of K in clinopyroxene, orthopyroxene, and the whole-rock sample, respectively. It is, however, not clear if all the K (and Cl) is hosted by phlogopite. There are coincident release peaks of K- and Cl-derived argon matching ^{37}Ar release from pyroxenes (Fig. 8a and b), and from EMPA we cannot preclude that clinopyroxene can host a significant proportion of the K (and Cl) detected in the clinopyroxene separate. Moreover, fluid inclusions could also influence the Cl budget. This may also explain the K/Cl ratios of pyroxene and whole-rock samples of 4·5, 12·6 and ~8, which are significantly lower than the EMPA-derived K/Cl ratio of phlogopite of 23 ± 3. Another possibility is that the K-derived ^{39}Ar in the pyroxene release peak is from mineral grains completely encapsulated in pyroxene. Such minerals were observed previously by Henjes-Kunst *et al.* (1990) and described in detail by Kaliwoda *et al.* (2007): intragranular Ba-pargasite and Ba-phlogopite are characteristic features of xenolith SA84-63. After formation of hydrous minerals, subsequent recrystallization caused the partial replacement of pargasite by clinopyroxene.

The olivine separate of SA84-63 is again similar to SA84-128/3 olivine, characterized by comparatively low Ar, K, Ca, and Cl contents and low $^{40}Ar/^{36}Ar$ ratios (Fig. 8c), much lower than in the pyroxene separates. The composition of the whole-rock sample of SA84-63 is dominated by clinopyroxene, for which we can calculate a modal abundance of 84%, using the Ca, K and Cl concentrations from EMPA (in agreement with observation under thin section). The phlogopite reservoir at intermediate temperatures is not well resolved.

Minor release peaks at low temperatures are also present in all the separates and the whole-rock sample of this xenolith. These are characterized by surprisingly high $^{40}Ar/^{36}Ar$ ratios of up to 2500 (Fig. 8). With increasing extraction temperature, the amount of mantle ^{40}Ar also increases and $^{40}Ar/^{36}Ar$ ratios rise to 6500 and 10 000 in clinopyroxene and orthopyroxene, respectively (Fig. 8a and b). Similar to SA84-128/3, argon from pyroxene has higher $^{40}Ar/^{36}Ar$ ratios than the hydrous phase (phlogopite with $^{40}Ar/^{36}Ar$ ratios of about 2000–5000). It follows that also in this case, even for seemingly 'pure' mineral separates, the argon isotope composition obtained by total fusion extractions is meaningless and that high-resolution stepwise heating is a necessary tool to constrain the mantle noble gas signature.

Comparison of pargasite lherzolite SA84-128/3 and olivine websterite SA84-63

When comparing the overall data for xenoliths SA84-63 and SA84-128/3 (see Table 1), we can conclude that phlogopite formation and incorporation of fluid inclusions in pyroxenes in SA84-63 (earlier metasomatism 1, <18 Myr ago) was obviously caused by a fluid source with relatively high $^{40}Ar/^{36}Ar$ ratios (up to 10 000). This fluid was distinctly different from the fluid triggering pargasite formation in SA84-128/3 with low $^{40}Ar/^{36}Ar$ ratios <400 (metasomatism 2, ~4 Myr ago). Moreover, the respective metasomatic agents also induced incorporation of fluid inclusions into pyroxenes of the two xenoliths, again with distinctly different $^{40}Ar/^{36}Ar$ ratios. Olivine was affected to only a very minor degree—its very low content of mantle argon makes it susceptible to late-stage incorporation of atmospheric argon, possibly additionally influenced by weathering (although we explicitly state here that olivine separates looked very fresh and clean). Atmospheric noble gas contamination and its incorporation into mantle rocks is still puzzling and enigmatic (e.g. Ballentine & Barfod, 2000; Harrison *et al.*, 2003). Weathering products, of course, contain atmospheric contaminants, but frequently atmosphere-type noble gases are observed even if no weathering is apparent. One cryptic mechanism called 'irreversible adsorption' was suggested by Niedermann & Eugster (1992) to explain atmospheric contaminants in extraterrestrial samples. Atmospheric noble gases were released even at surprisingly high extraction temperatures. As olivine mostly contains lower concentrations of noble gases in mantle xenoliths, even low amounts of such atmospheric contaminants would be recognizable. However, a discussion of this effect is beyond the scope of this paper.

Although some minor amounts of atmospheric argon could have been incorporated by the effects mentioned above, we consider that the atmospheric argon components incorporated into the amphiboles and pyroxenes are source effects, because there is a clear correlation of $^{40}Ar/^{36}Ar$ ratios and the composition of the metasomatic agents (see the sections below on mantle metasomatism and accompanying volatile agents). Such a correlation was previously observed for different generations of amphiboles from Zabargad peridotites (Agrinier *et al.*, 1993; Trieloff *et al.*, 1997) that displayed distinct argon, hydrogen and Sr isotope compositions.

Xenolith whole-rock analyses

For the remaining four weakly metasomatized xenoliths from Harrat Uwayrid and from Harrat Al Birk, only whole-rock samples were analysed. All xenoliths are

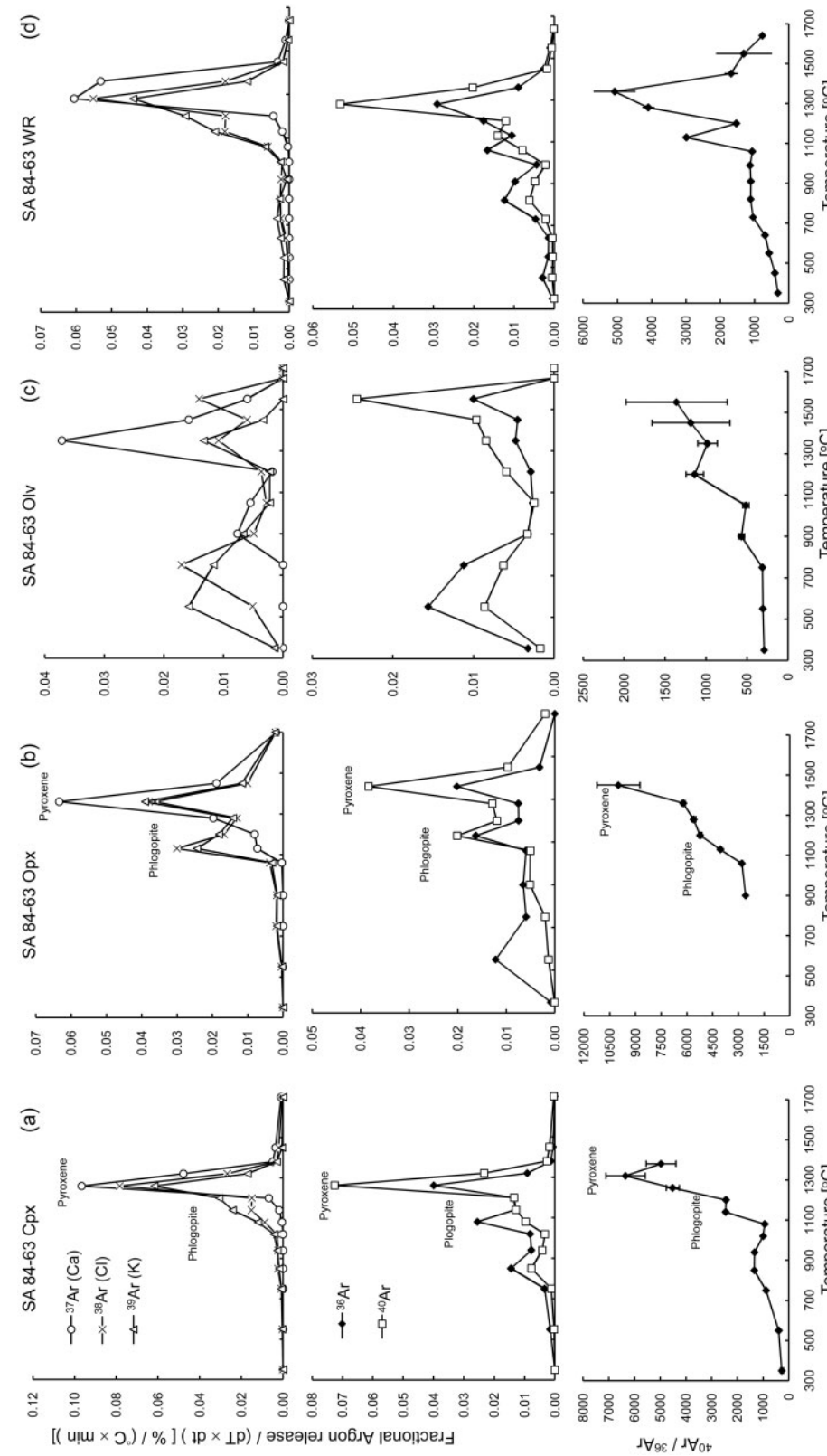

Fig. 8. Degassing patterns of argon isotopes and $^{40}Ar/^{36}Ar$ ratios vs extraction temperature for SA84-63 clinopyroxene (a), orthopyroxene (b), olivine (c) and whole-rock (d). The peaks at high temperature (from pyroxene) and at intermediate temperature are better resolved than in SA84-128/3.

characterized by complex release patterns (Fig. 9). Release peaks of Ca-derived ^{37}Ar related to pyroxene are recognizable in all of them; however, amphibole release peaks (^{39}Ar and ^{38}Ar from K and Cl, respectively) seem to be present only in xenolith SA84-123, for which K data (Table 2) constrain the amphibole abundance to less than a few per mil. For SA84-38, minor amphibole could be present, judging from a sharp peak of ^{40}Ar and $^{40}Ar/^{36}Ar$ at 1100°C. Low-temperature peaks are common in all samples. In the case of xenolith SA84-38, the broad release between 500 and 1300°C indicates argon extraction from glass. Based on the EMPA-derived potassium content of the glass (~700–1100 ppm), we can calculate a modal glass abundance of about 1·3–2·0 wt % in this sample. In contrast, the broad low-temperature release of K- and Cl-derived argon from (glass-free) xenolith SA84-123 is more likely to be due to alteration phases such as montmorillonite and smectite, consistent with the very low $^{40}Ar/^{36}Ar$ ratios that are indistinguishable from atmospheric composition. In general, the low degree of metasomatism of all these samples is clearly reflected by the low K and Cl concentrations, the low abundance of amphibole and/or glass, the low content of ^{36}Ar and mantle ^{40}Ar, and the low abundance of fluid inclusions. Only SA87-6/9 has abundant fluid inclusions in pyroxene, which results in relatively high $^{40}Ar/^{36}Ar$ ratios in many extractions (average ~3100, and up to 4400; see Table 1). The other whole-rock samples are poor in fluid inclusions, hydrous minerals or glass, and have average $^{40}Ar/^{36}Ar$ ratios of <1100, although a very few extractions still have a memory of a high $^{40}Ar/^{36}Ar$ mantle origin, predominantly in the pyroxene or amphibole release regimes. Again, olivine (releasing argon at 1500–1700°C) does not seem to contain significant amounts of mantle argon, although minor amounts of mantle argon could remain undegassed even at high temperatures of 1700°C. The variability of argon isotope composition between minerals again can be interpreted as the result of fluid–rock interaction with isotopically different fluids during magmatic evolution, except for olivine, for which alteration processes at surface conditions could possibly introduce atmospheric argon.

Argon distribution between phases

Here we briefly summarize the argon concentrations in the studied mantle minerals. Because argon concentrations in a mineral reflect those of the argon sources, the concentration of argon cannot generally be considered as a characteristic of the mineral unless the interacting magma source was comparable. As our samples were derived at different times and trapped argon from different sources, the relative argon concentrations should not be overinterpreted in terms of the general characteristics of the respective minerals.

Olivine–pyroxene

Using the argon content in mineral separates and in different temperature release regimes, we calculated the relative distribution of atmospheric and mantle argon between phases. Generally, the concentration of both mantle ^{40}Ar and atmospheric ^{36}Ar is significantly lower in olivine than in pyroxene, but the average concentration ratio $^{36}Ar(olivine)/^{36}Ar(pyroxene)$ is 2–3 times higher than for $^{40}Ar_{mantle}$. This results in much lower $^{40}Ar/^{36}Ar$ ratios in olivine when compared with pyroxene. Obviously, the olivine grains have captured considerably lower amounts of mantle argon than pyroxene, either in fluid inclusions or in the mineral lattice, but the susceptibility of olivine to subsequent atmospheric contamination processes is higher, causing a modification of its argon isotopic composition. It should be kept in mind that this reasoning applies only if significant amounts of mantle olivine remained undegassed, as discussed above.

Orthopyroxene–clinopyroxene

The concentration of mantle ^{40}Ar and atmospheric ^{36}Ar in clinopyroxene and orthopyroxene is approximately equal, which is reflected by similar $^{40}Ar/^{36}Ar$ ratios in these minerals (if separated from the same xenolith).

Hydrous phases

The distribution of argon in hydrous phases is more complicated: when amphibole is exceptionally abundant, as in SA84-128/3, it has an ^{36}Ar concentration similar to pyroxene, but a lower ^{40}Ar concentration. If amphibole or phlogopite are at the <1% abundance level, as in SA84-63 or SA84-123, calculated concentrations of mantle ^{40}Ar are generally 2–3 times higher than in pyroxene. However, the concentration of atmosphere-derived ^{36}Ar is a factor of up to 20 higher in hydrous phases, resulting in $^{40}Ar/^{36}Ar$ ratios lower than in pyroxene (except for SA84-38).

Summary

Overall, pyroxene is the phase that preserves the highest proportion of mantle argon. Most probably, a significant part of this argon is from a subcontinental mantle source that has a $^{40}Ar/^{36}Ar$ ratio similar to the shallow MORB mantle reservoir (>28 000). A possible contribution of plume-type argon in Arabian mantle xenoliths has been discussed by Hopp *et al.* (2004, 2007). Pyroxene presumably also trapped argon from the fluids that caused the formation of hydrous minerals during mantle metasomatism. These fluids were from different sources, characterized by distinct proportions of mantle and atmospheric argon. For example, secondary intergranular amphiboles formed in xenoliths SA84-128/3 and SA84-123 are characterized by distinctly low $^{40}Ar/^{36}Ar$ ratios, indicating a different fluid from that causing pargasite and phlogopite formation in SA84-63.

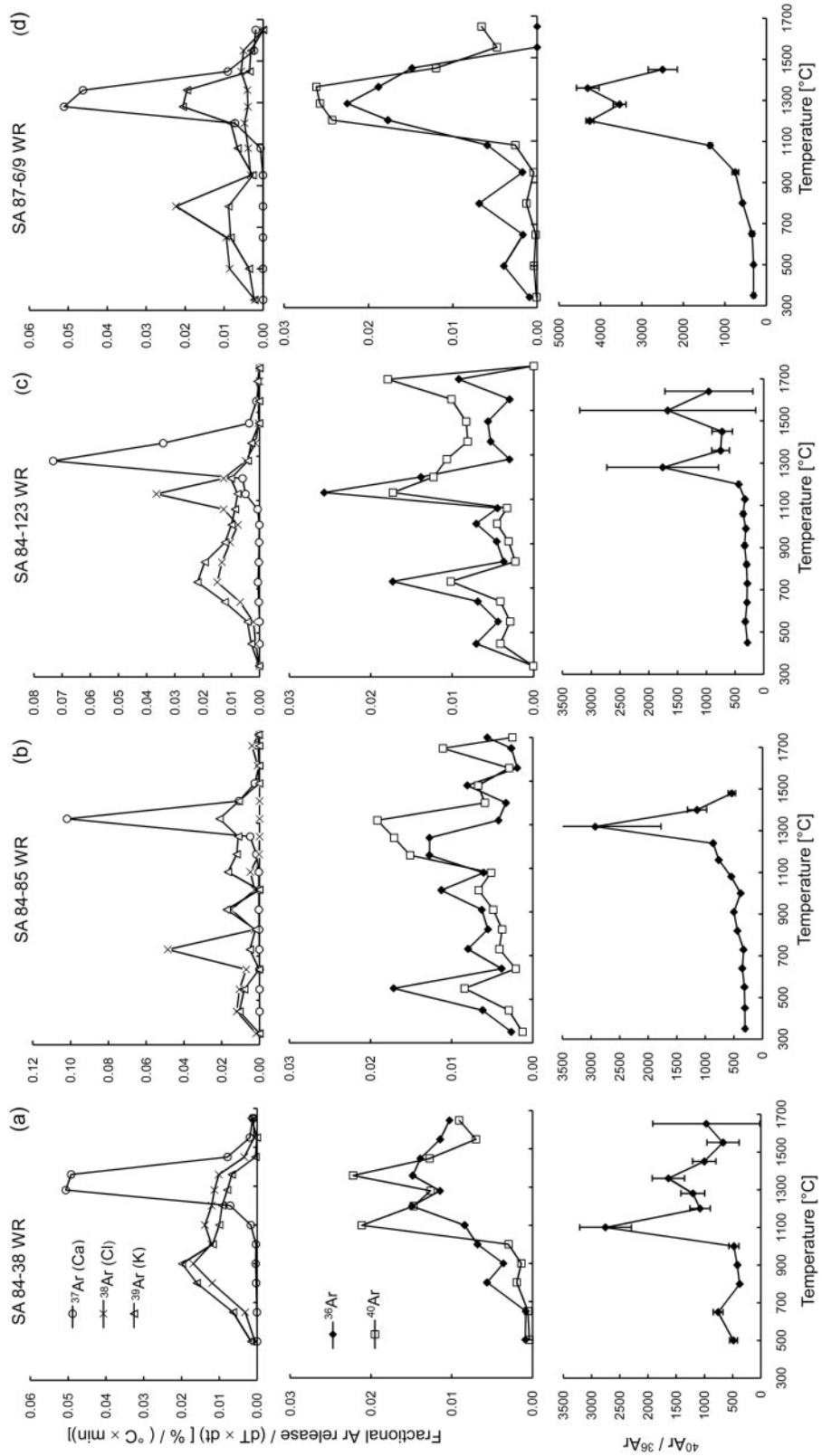

Fig. 9. Degassing patterns of argon isotopes and $^{40}Ar/^{36}Ar$ ratios vs extraction temperature for whole-rock samples SA84-38 (a), SA84-85 (b), SA84-123 (c), and SA87-6/9 (d).

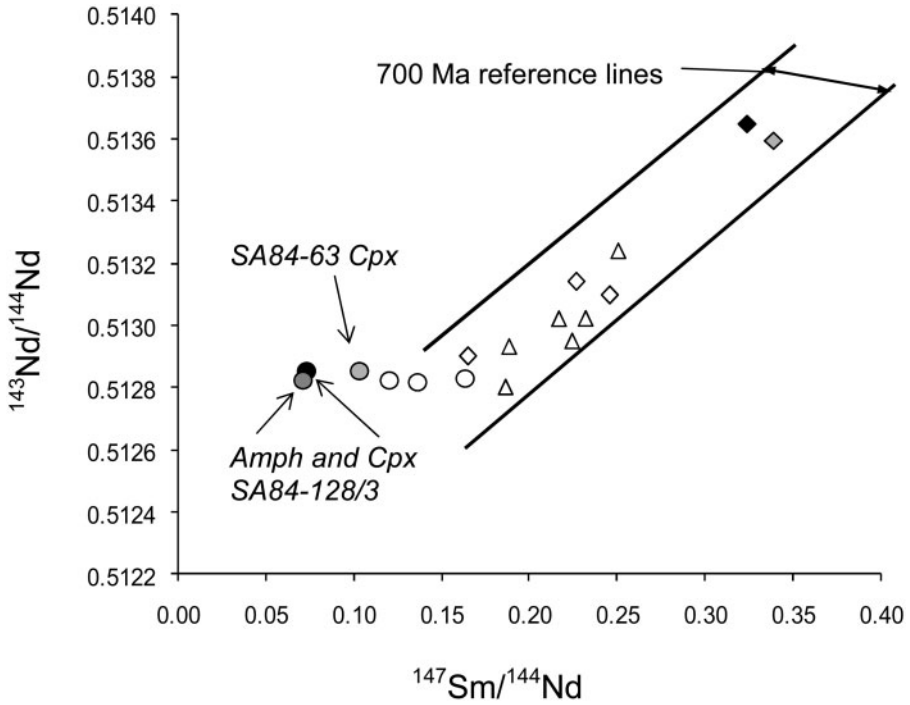

Fig. 10. Sm–Nd isochron diagram for clinopyroxenes and secondary intergranular amphibole from Arabian mantle xenoliths (after Henjes-Kunst *et al.*, 1990). Diamonds, anhydrous xenoliths (grey, SA84-85; black, SA84-123); circles, metasomatically overprinted xenoliths (including SA84-128/3 and SA84-63); triangles, Al Birk xenoliths. Filled symbols indicate samples for which argon isotope composition was determined in this study.

Chronology and nature of mantle metasomatism recorded by Saudi Arabian xenoliths

Spinel-bearing mantle xenoliths from Cenozoic volcanic fields (harrats) of the Arabian peninsula record the chemically and isotopically heterogeneous nature of the lithospheric mantle beneath the region. Xenoliths largely unaffected by metasomatism form a linear array in a Sm–Nd isochron diagram (Fig. 10), possibly reflecting a fractionation event during the Pan-African about 700 Myr ago (Henjes-Kunst *et al.*, 1990). Some xenoliths, however, contain amphibole and/or phlogopite, and their minerals record isotopic and/or incompatible trace element evidence for younger metasomatic overprints (e.g. Brueckner *et al.*, 1988; Henjes-Kunst *et al.*, 1990; Blusztajn *et al.*, 1995; Baker *et al.*, 1998, 2002).

As indicated by our ^{40}Ar–^{39}Ar results, 4 Ma is a reasonable age constraint on the formation of intergranular amphibole in pargasite lherzolite SA84-128/3. A relatively young age (of a few million years) was also inferred from Rb–Sr systematics of amphibole–clinopyroxene pairs in this and other xenoliths (Henjes-Kunst *et al.*, 1990). Moreover, in xenolith SA84-63, phlogopite and clinopyroxene have similar $^{87}Sr/^{86}Sr$, although phlogopite has a much higher $^{87}Rb/^{86}Sr$, suggesting also a young age of no more than a few million years (Henjes-Kunst *et al.*, 1990). This conclusion is independently supported by our ^{40}Ar–^{39}Ar data on Ba-phlogopite from this xenolith; an upper limit of the formation age is $16{\cdot}6 \pm 1{\cdot}8$ Ma (Table 1).

In terms of their Sm–Nd systematics, clinopyroxene and amphibole fractions from metasomatized xenoliths form a horizontal, linear array in a Sm–Nd isochron diagram (Fig. 10). Remarkably, SA84-128/3 amphibole also plots on this array, and is indistinguishable in both $^{143}Nd/^{144}Nd$ and $^{147}Sm/^{144}Nd$ from the clinopyroxene of SA84-128/3 (Fig. 10). This is a strong hint that the various metasomatic events recorded by the xenoliths from the various volcanic fields were closely related in time and composition, possibly resulting from a similar fluid source, probably as different pulses from the same parent fluid, or differently evolved composition. This also implies that recrystallization after pargasite and phlogopite formation in SA84-63 lasted no more than a few million years, probably enhanced by the presence of fluid phases. Obviously, weakly metasomatized xenoliths, such as SA84-85 and SA84-123, were not overprinted by the late REE-rich fluid(s) and still 'memorize' a 700 Ma age of a Pan-African fractionation event in their Sm–Nd system (Fig. 10) (Henjes-Kunst *et al.*, 1990).

Recent mantle metasomatism is also indicated by noble gas analyses of some of these xenoliths. SA87-6/9, SA84-38

and SA84-63 contain mantle helium ($^4He/^3He$ between 90 000 and 120 000), mantle neon ($^{20}Ne/^{22}Ne$ up to 11·2), and mantle argon ($^{40}Ar/^{36}Ar$ up to 10 000) from both the subcontinental lithospheric mantle as well as contributions from the Afar deep mantle plume, incorporated during mantle metasomatism less than 30 Myr ago (Hopp, 2002; Hopp *et al.*, 2004, 2007), triggered by syn- or post-magma tectonic events associated with the initialization of the Afar plume.

A striking result of this study is the contrasting $^{40}Ar/^{36}Ar$ ratios in different rocks and phases, although the Sm–Nd and Rb–Sr isotope systems indicate rather similar metasomatic fluids; this may simply be related to the atmophile (non-lithophile) nature of argon and its high susceptibility to record imprints from atmospheric argon derived from meteoric fluids. Specifically, the high $^{40}Ar/^{36}Ar$ ratios of SA84-63 are obviously characteristic of the melt that formed phlogopite (0·3% modal abundance) and/or CO_2 fluids resulting possibly from melt exsolution and incorporated into SA84-63 pyroxene. Remarkably, high $^{40}Ar/^{36}Ar$ ratios were also observed for intergranular amphibole (<0·3% modal abundance) in the less metasomatized xenolith SA84-38. Apparently, if the modal abundance of hydrous phases is low, then $^{40}Ar/^{36}Ar$ ratios are high; that is, the contribution of atmospheric argon is low (obviously regardless of metasomatism intensity or timing). In contrast, in all cases where amphibole is abundant [SA84-128/3 (20%) and hornblende megacrysts], it has low $^{40}Ar/^{36}Ar$ ratios. As a feasible explanation we consider that the formation of abundant amphibole requires the presence of sufficient amounts of water, which cannot be supplied from the mantle, but are ultimately derived from the surface; for example, meteoric water or seawater that is assimilated by crustal magma chambers. We consider much less likely the possibility that large amounts of amphibole could trap a certain, limited amount of mantle argon in lower average concentrations. An argument against this possibility is the correlation of argon, hydrogen and Sr isotopic composition previously observed for different generations of Zabargad amphiboles (Agrinier *et al.*, 1993; Trieloff *et al.*, 1997).

In any case it should be kept in mind that the atmosphere—and surface-sited rocky or fluid reservoirs—are the major reservoirs for terrestrial noble gases and that modest contributions from these reservoirs (either to magma sources or samples) will readily modify the original mantle argon isotopic signature. We finally emphasize here that mantle metasomatism is capable of enriching and transporting mantle noble gases and depositing them in metasomatic phases, whereas the primary mantle noble gas content of the major minerals (lattice hosted) appears rather low and is more difficult to quantify, and is also more susceptible to atmospheric contamination.

Correlations of argon and other volatile elements (K, Cl)

Figure 11a and b shows $^{40}Ar/^{36}Ar$ vs $Cl/^{36}Ar$ and $^{40}Ar^*/Cl$ vs Cl. For comparison, data for African and Canadian diamonds, African mantle xenoliths (Johnson *et al.*, 2000), Loihi and MORB glasses (Trieloff *et al.*, 2003) and Zabargad peridotite samples (Trieloff *et al.*, 1997) are also plotted. The Uwayrid xenoliths show a wide range of $^{40}Ar^*/Cl$ and $Cl/^{36}Ar$ ratios and Cl concentrations, but rather uniform K/Cl ratios (with the exception of SA84-85 and SA84-38). The data could be interpreted as the result of three- or four-component mixing between atmosphere, shallow mantle (MORB-type and/or subcontinental lithospheric mantle) and late metasomatic agents. The last are, for example, represented by the composition of secondary intergranular amphibole in SA84-128/3 and also by the composition of Zabargad amphibole Z28 (Trieloff *et al.*, 1997), and tend to be significantly influenced by an atmospheric component. It should be noted that hornblende megacrysts from Harrat Uwayrid have volatile compositions similar to SA84-128/3 amphibole. They are also characterized by very low $^{40}Ar^*/Cl$, rather high $Cl/^{36}Ar$ ratios and high Cl concentrations. A possible explanation could be the addition of seawater or saline water from evaporites to the source of the metasomatizing fluids. For example, evaporites occur on Zabargad Island, and amphibole formation by interaction with seawater seems to be a possibility (Agrinier *et al.*, 1993; Trieloff *et al.*, 1997). In the case of the Uwayrid amphiboles, which are <4 Myr old, the opening of the Red Sea starting at ~5 Myr ago could have induced seawater infiltration into deep crustal layers. The atmospheric contaminating agent could also have been added previously to the source of the metasomatizing fluids via ancient seawater alteration during Pan-African times. It should be noted that the Cl concentration in Zabargad amphibole is about 10 times higher and the K/Cl ratio is almost two orders of magnitude lower when compared with the Uwayrid amphiboles. The $Cl/^{36}Ar$ ratios vary widely, up to 5×10^8 in amphibole SA84-128/3 and $6{\cdot}4 \times 10^8$ in Zabargad amphibole (Fig. 11a). These values are more than two orders of magnitude higher than the ratio in seawater. They could be reasonably explained by chemical fractionation, as growing amphibole crystals preferentially incorporate chlorine rather than argon. This process is also shown in Fig. 11b: the higher the Cl content, the lower $^{40}Ar^*/Cl$ ratio in the samples.

We note from petrographic observations (Kaliwoda *et al.*, 2007) of melt inclusions that a formation depth of the xenoliths of *c.* 35–40 km is inferred. This means that the amphiboles could have been formed both at the top of the shallow mantle and/or in the lower layers of the lower crust. Another point is that amphibole and other Cl-bearing phases were probably formed before the

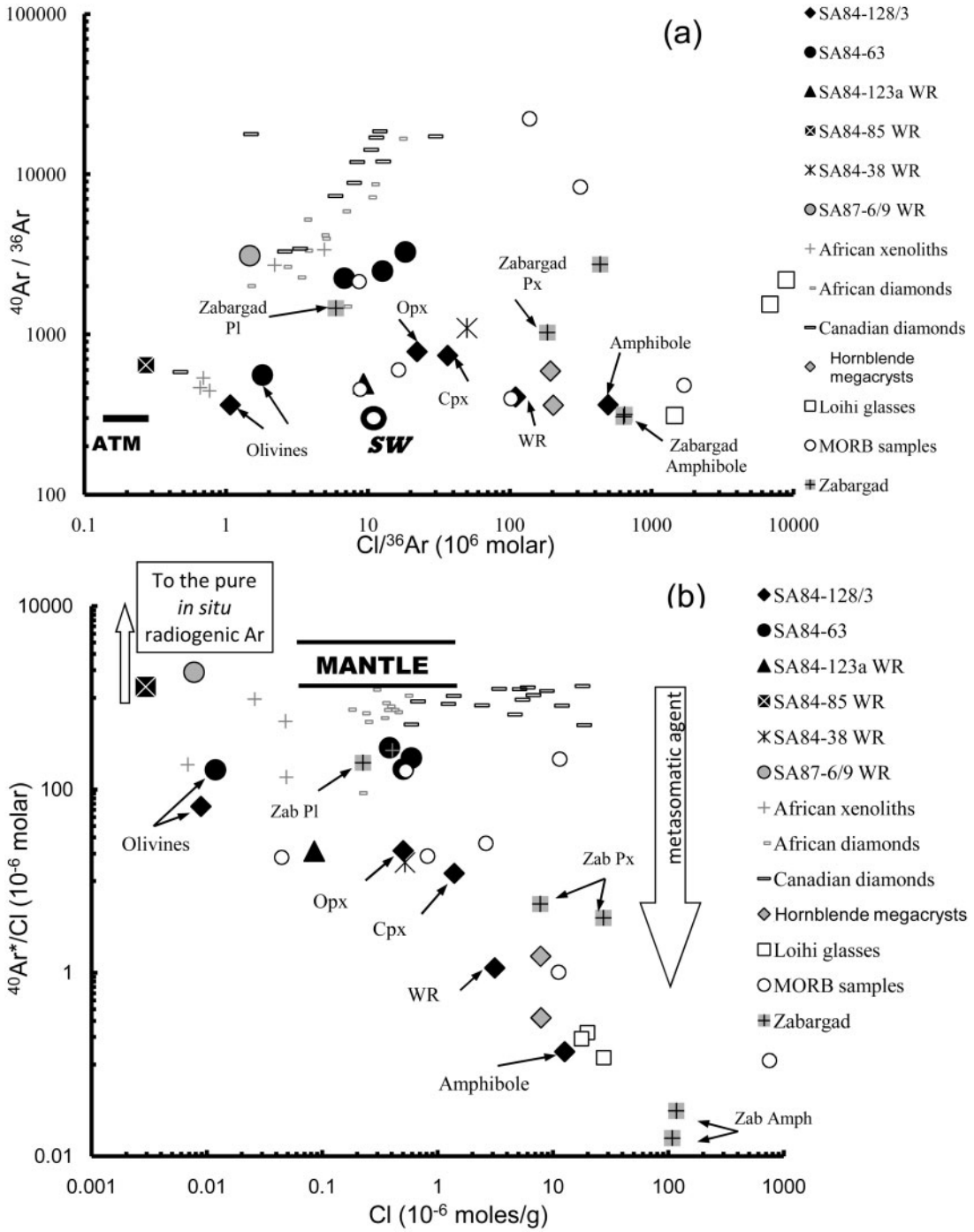

Fig. 11. (a) $^{40}Ar/^{36}Ar$ vs $Cl/^{36}Ar$ for Arabian mantle xenoliths. For comparison, data for African and Canadian diamonds, African mantle xenoliths (Johnson *et al.*, 2000), Loihi and MORB glasses (Trieloff *et al.*, 2003) and Zabargad samples (Trieloff *et al.*, 1997) are also plotted. SW = seawater (b) Dependence of $^{40}Ar^*/Cl$ ratios on Cl concentrations in Arabian mantle xenoliths and African and Canadian diamonds, African xenoliths (Johnson *et al.*, 2000), Loihi and MORB glasses (Trieloff *et al.*, 2003) and Zabargad samples (Trieloff *et al.*, 1997). The wide range of $^{40}Ar^*/Cl$ ratios and Cl concentrations in Uwayrid and Zabargad samples reflects the extent of the late metasomatic overprint. Generally, for higher Cl contents we observe lower $^{40}Ar^*/Cl$ ratios in metasomatized Uwayrid and Zabargad samples. This reflects the chemical fractionation process during amphibole formation, as growing amphibole crystals preferentially incorporate chlorine when compared with other phases.

incorporation of some fluids, as fluid inclusion trails cross-cut the amphibole (Fig. 2b). Unfortunately, it is not possible to distinguish between the time of amphibole formation and that of the incorporation of secondary fluids—the most probable phase bearing atmosphere-type argon.

In contrast, the volatile and argon isotope compositions of xenolith SA84-63, which was not subjected to the late metasomatism 2 (see above and Henjes-Kunst *et al.*, 1990), are closely similar to the compositions of upper mantle samples reported by Johnson *et al.* (2000). There is a well-defined trend from the metasomatism 2 end-member to the low chlorine and high $^{40}Ar^*/Cl$ area (Fig. 11b) of the uncontaminated mantle source, reflected also in the composition of SA84-128/3 amphibole–whole-rock–clinopyroxene–orthopyroxene. In principle, the same trend is also followed by the sequence of Zabargad amphibole–pyroxene–plagioclase (Fig. 11b). In the $^{40}Ar/^{36}Ar$ vs $Cl/^{36}Ar$ plot the correlation is not as well defined, but still recognizable (Fig. 11a). In both diagrams the olivine separates plot apart from the main trends, possibly reflecting a stronger contamination effect by atmospheric argon as a result of alteration (or weathering), and a much less pronounced affinity for chlorine.

The volatile elemental and argon isotope compositions of the Uwayrid xenoliths suggest a strong difference between the metasomatic agents. The difference in argon isotope composition points to the presence of an almost pristine upper mantle source beneath the Saudi Arabian region (as inferred from the metasomatic minerals of SA84-63 xenolith), whereas the subsequent tectonic evolution was strongly influenced by atmosphere-type argon. Argon, chlorine and potassium relationships indicate that the most feasible contaminating agent was saline water introduced into the mantle source (or intermediate magma chamber).

SUMMARY AND CONCLUSIONS

We have used high-resolution stepwise heating ^{40}Ar–^{39}Ar analyses to study the geochemical behaviour of argon isotopes during mantle metasomatism and its chronology, including associated effects such as the enrichment of the main mineral phases ('cryptic metasomatism') and the formation of accessory phases such as amphibole ('modal metasomatism') on the argon isotope composition of mantle xenoliths.

Xenoliths from the Uwayrid volcanic field have distinct argon isotope compositions that reflect interactions with isotopically and genetically different fluids and/or melts during different episodes of recent mantle metasomatism (see Henjes-Kunst *et al.*, 1990). Contrary to the Sm–Nd and Rb–Sr isotope systematics, the volatile element (K, Ar, Cl) and argon isotope compositions of the Uwayrid xenoliths suggest a strong difference between the sources of the metasomatic agents.

High $^{40}Ar/^{36}Ar$ ratios (up to 10 500) in minerals of xenolith SA84-63 point to the presence of a relatively pure mantle argon component from the subcontinental Saudi Arabian lithospheric mantle. Other metasomatic phases are characterized by very low $^{40}Ar/^{36}Ar$ ratios, indicating that subsequent evolution was strongly influenced by atmosphere-type argon. Argon, chlorine and potassium relationships indicate that the most feasible contaminating agent was saline water introduced into the mantle source (or intermediate magma chamber).

Hornblende megacrysts SA84-64 and SA84-42B (formed about 1·1 and 1·7 Myr ago) also suggest significant influence of a low $^{40}Ar/^{36}Ar$ component during the late stages of magmatic evolution. Their K, Cl, Ar inventory and argon isotope composition also support the idea of the presence of saline water as a contaminating agent.

A reasonable age constraint on the formation of secondary intergranular Cr-pargasite in the SA84-128/3 xenolith, and implicitly on the age of late mantle metasomatism, is ~4 Ma. Such a relatively young age is consistent with Rb–Sr and Sm–Nd estimates of the age of a late metasomatic event in the Saudi Arabian region (Henjes-Kunst *et al.*, 1990).

The study of argon distribution between mineral phases has shown that pyroxenes and amphiboles in mantle xenoliths have the highest concentrations of mantle argon (up to an order of magnitude higher than for olivine), making them the most suitable candidates to study mantle metasomatic processes by means of noble gas isotopes.

ACKNOWLEDGEMENTS

We thank W. H. Schwarz for helpful discussions. We are indebted to reviewers Ray Burgess and Ichiro Kaneoka, whose comments effectively improved the paper. We thank Forschungszentrum Geesthacht (GKSS) for access to neutron irradiation facilities.

FUNDING

A.I.B., M.T. and E.V.K. acknowledge support by the Deutsche Forschungsgemeinschaft via grant numbers TR333/3 and 4, 436 RUS 17/100/02, and 436 RUS 17/91/01. A.I.B. acknowledges support by Russian Foundation for Fundamental Investigations (RFFI grant N09-05-00678a).

SUPPLEMENTARY DATA

Supplementary data for this paper are available at *Journal of Petrology* online.

REFERENCES

Agrinier, P., Mével, C., Bosch, D. & Javoy, M. (1993). Metasomatic hydrous fluids in amphibole peridotites from Zabargad Island (Red Sea). *Earth and Planetary Science Letters* **120**, 187–205.

Allègre, C. J., Staudacher, Th. & Sarda, P. (1986). Rare gas systematics: Formation of the atmosphere, evolution and structure of the Earth's mantle. *Earth and Planetary Science Letters* **81**, 127–150.

Al-Mishwat, A. T. & Nasir, S. J. (2004). Composition of the lower crust of the Arabian Plate: a xenolith perspective. *Lithos* **72**, 45–72.

Baker, J. A., Snee, L. W. & Menzies, M. A. (1996). A brief Oligocene period of flood volcanism in Yemen: Implications for the duration and rate of continental flood volcanism at the Afro-Arabian triple junction. *Earth and Planetary Science Letters* **138**, 39–55.

Baker, J. A., Chazot, G., Menzies, M. A. & Thirlwall, M. F. (1998). Metasomatism of the shallow mantle beneath Yemen by the Afar plume: implications for mantle plumes, flood volcanism, and intraplate volcanism. *Geology* **26**, 431–434.

Baker, J. A., Chazot, G., Menzies, M. A. & Thirlwall, M. (2002). Lithospheric mantle beneath Arabia: a Pan-African protolith modified by the Afar and older plumes, rather than a source of continental flood volcanism. In: Menzies, M. A., Klemperer, S. L., Ebinger, C. J. & Baker, J. (eds) *Volcanic Rifted Margins. Geological Society of America, Special Papers* **362**, 65–80.

Ballentine, C. J. & Barfod, D. (2000). The origin of air-like noble gases in MORB and OIB. *Earth and Planetary Science Letters* **180**, 39–48.

Blusztajn, J., Hart, S. R., Shimizu, N. & McGuire, A. V. (1995). Trace-element and isotopic characteristics of spinel peridotite xenoliths from Saudi Arabia. *Chemical Geology* **123**, 53–65.

Bohannon, R. G., Naeser, C. W., Schmidt, D. L. & Zimmermann, R. A. (1989). The timing of uplift, volcanism, and rifting peripheral to the Red Sea: a case for passive rifting? *Journal of Geophysical Research* **94**, 1683–1701.

Brereton, N. R. (1970). Corrections for interfering isotopes in the ^{40}Ar–^{39}Ar dating method. *Earth and Planetary Science Letters* **8**, 427–433.

Brey, G. P. & Köhler, T. (1990*a*). Geothermobarometry on four-phase lherzoliths I. Experimental results from 10 to 60 kb. *Journal of Petrology* **31**, 1313–1352.

Brey, G. P. & Köhler, T. (1990*b*). Geothermobarometry on four-phase lherzoliths II. New thermobarometers, and practical assessment of existing thermobarometers. *Journal of Petrology* **31**, 1353–1378.

Brueckner, H. K., Zindler, A., Seyler, M. & Bonatti, E. (1988). Zabargad and the isotopic evolution of the sub-Red Sea mantle and crust. *Tectonophysics* **150**, 163–176.

Buikin, A., Trieloff, M., Hopp, J., Althaus, T., Korochantseva, E., Schwarz, W. H. & Altherr, R. (2005*a*). Noble gas isotopes suggest deep mantle plume source of late Cenozoic mafic alkaline volcanism in Europe. *Earth and Planetary Science Letters* **230**, 143–162.

Buikin, A., Trieloff, M. & Ryabchikov, I. D. (2005*b*). Ar-40–Ar-39 dating of a phlogopite-bearing websterite: Evidence for ancient metasomatism in the subcontinental lithospheric mantle under the Arabian Shield? *Doklady Earth Sciences* **400**, 44–48.

Camp, V. E. & Roobol, M. G. (1989). The Arabian continental alkali basalt province: Part I. Evolution of Harrat Rahat, Kingdom of Saudi Arabia. *Geological Society of America Bulletin* **101**, 71–95.

Camp, V.E. & Roobol, M.J. (1991). The Arabian continental alkali basalt province: Part II. Evolution of Harrats Khaybar, Ithnayn, and Kura, Kingdom of Saudi Arabia. *Geological Society of America Bulletin* **104**, 363–391.

Camp, V.E. & Roobol, M.J. (1992). Upwelling asthenosphere beneath Western Arabia and its regional implications. *Journal of Geophysical Research* **97**, 15255–15271.

Coleman, R.G., Gregory, R.T. & Brown, G. F. (1983). Cenozoic volcanic rocks of Saudi Arabia. Saudi Arabian Deputy Minister of Mineral Resources. Open File Report USGS-OF93. 82 pp.

Coulié, E., Quideleur, X., Gillot, P.-Y., Courtillot, V., Lefèvre, J.-C. & Chiesa, S. (2003). Comparative K–Ar and Ar/Ar dating of Ethiopian and Yemenite Oligocene volcanism: implications for timing and duration of the Ethiopian traps. *Earth and Planetary Science Letters* **206**, 477–492.

Courtillot, V., Jaupart, C., Manighetti, I., Tapponier, P. & Besse, J. (1999). On causal links between flood basalts and continental breakup. *Earth and Planetary Science Letters* **166**, 177–195.

Dunai, T. J. & Baur, H. (1995). Helium, neon, and argon systematics of the European subcontinental mantle: Implications for its geochemical evolution. *Geochimica et Cosmochimica Acta* **59**, 2767–2783.

Harrison, D., Burnard, P. G., Trieloff, M. & Turner, G. (2003). Resolving atmospheric contaminants in mantle noble gas analyses. *Geochemistry, Geophysics, Geosystems* **4**, paper no. 1023 (2002GC000325).

Henjes-Kunst, F., Altherr, R. & Baumann, A. (1990). Evolution and composition of the lithospheric mantle underneath the western Arabian peninsula: Constraints from Sr–Nd isotope systematics of mantle xenoliths. *Contributions to Mineralogy and Petrology* **105**, 460–472.

Hofmann, A. W. (1997). Mantle geochemistry: The message from oceanic volcanism. *Nature* **385**, 219–229.

Hofmann, C., Courtillot, V., Féraud, G., Rochette, P., Yirgu, G., Ketefo, E. & Pik, R. (1997). Timing of the Ethiopian flood basalt event and implications for plume birth and global change. *Nature* **389**, 838–841.

Honda, M., McDougall, I., Patterson, D. B., Doulgeris, A. & Clague, D. A. (1991). Possible solar noble-gas component in Hawaiian basalts. *Nature* **349**, 149–151.

Hopp, J. (2002). Die Isotopenzusammensetzung von Helium, Neon und Argon in ultramafischen Gesteinen des subkontinentalen lithosphärischen Mantels im Gebiet des Roten Meeres, Doctoral thesis, University of Heidelberg, 131 pp.

Hopp, J. & Trieloff, M. (2005). Refining the noble gas record of the Réunion mantle plume source: implications on mantle geochemistry. *Earth and Planetary Science Letters* **240**, 573–588.

Hopp, J., Trieloff, M. & Altherr, R. (2004). Neon isotopes in mantle rocks from the Red Sea region reveal large-scale plume–lithosphere interaction. *Earth and Planetary Science Letters* **219**, 61–76.

Hopp, J., Trieloff, M., Buikin, A. I., Korochantseva, E. V., Schwarz, W. H., Althaus, T. & Altherr, R. (2007). Heterogeneous mantle argon isotope composition in the subcontinental lithospheric mantle beneath the Red Sea region. *Chemical Geology* **240**, 36–53, doi:10.1016/j.chemgeo.2007.01.004.

Jessberger, E. K., Dominik, B., Staudacher, Th. & Herzog, G. F. (1980). ^{40}Ar–^{39}Ar ages of Allende. *Icarus* **42**, 380–405.

Johnson, L. H., Burgess, R., Turner, G., Milledge, H. J. & Harris, J. W., J. W. (2000). Noble gas and halogen geochemistry of mantle fluids: Comparison of African and Canadian diamonds. *Geochimica et Cosmochimica Acta* **64**, 717–732.

Kaliwoda, M. (2004). Mantel-Xenolithe des Harrat Uwayrid (Saudi Arabien): Archive der stofflichen thermischen Entwicklung des lithosphärischen Erdmantels im Bereich eines passiven Kontinentalrandes, PhD thesis, University of Heidelberg.

Kaliwoda, M., Altherr, R. & Meyer, H. P. (2007). Composition and thermal evolution of the lithospheric mantle beneath the Harrat Uwayrid, eastern flank of the Red Sea rift (Saudi Arabia). *Lithos* **99(1–2)**, 105–120.

Köhler, T. P. & Brey, G. P. (1990). Calcium exchange between olivine and clinopyroxene calibrated as geothermobarometer for natural peridotites from 2 to 60 kb with applications. *Geochimica et Cosmochimica Acta* **54**, 2375–2388.

Kuo, L. C. & Essene, E. J. (1986). Petrology of spinel harzburgite xenoliths from the Kishb Plateau, Saudi Arabia. *Contributions to Mineralogy and Petrology* **93**, 335–346.

Kurat, G., Palme, H., Embey-Isztin, A., Touret, J., Ntaflos, T., Spettel, B., Brandstätter, F., Palme, C., Dreibus, G. & Prinz, M. (1993). Petrology and geochemistry of peridotites and associated vein rocks of Zabargad island, Red Sea, Egypt. *Mineralogy and Petrology* **48**, 309–341.

Marty, B., Pik, R. & Gezahegn, Y. (1996). Helium isotopic variations in Ethiopian plume lavas: nature of magmatic sources and limit on lower mantle contribution. *Earth and Planetary Science Letters* **144**, 223–237.

Niedermann, S. & Eugster, O. (1992). Noble gases in lunar anorthositic rocks 60018 and 65315: Acquisition of terrestrial krypton and xenon indicating an irreversible adsorption process. *Geochimica et Cosmochimica Acta* **56**, 493–509.

McGuire, A. V. (1987). The mantle beneath the Red Sea margin: xenoliths from western Saudi Arabia. In: Bonatti, E. (ed.) *Zabargad Island and the Red Sea Rift. Tectonophysics* **150**, 101–119.

McGuire, A. V. (1988). Petrology of mantle xenoliths from Harrat al Kishb: The mantle beneath western Saudi Arabia. *Journal of Petrology* **29**, 73–92.

McGuire, A. V. & Stern, R. J. (1993). Granulite xenoliths from western Saudi Arabia: the lower crust of the late Precambrian Arabian–Nubian Shield. *Contributions to Mineralogy and Petrology* **114**, 395–408.

Moreira, M., Kunz, J. & Allègre, C. J. (1998). Rare gas systematics in popping rock: Isotopic and elemental compositions in the upper mantle. *Science* **279**, 1178–1181.

Ozima, M. & Podosek, F. A. (2002). *Noble Gas Geochemistry*, 2nd edn. Cambridge: Cambridge University Press, 286 p.

Pik, R., Deniel, C., Coulon, C., Yirgu, G. & Marty, B. (1999). Isotopic and trace element signatures of Ethiopian flood basalt: evidence for plume–lithosphere interactions. *Geochimica et Cosmochimica Acta* **63**, 2263–2279.

Poreda, R. J. & Farley, K. A. (1992). Rare gases in Samoan xenoliths. *Earth and Planetary Science Letters* **113**, 129–144.

Scarsi, P. & Craig, H. (1996). Helium isotope ratios in Ethiopian Rift basalts. *Earth and Planetary Science Letters* **144**, 505–516.

Schaeffer, G. A. & Schaeffer, O. A. (1977). ^{40}Ar–^{39}Ar ages of lunar rocks. *Proceedings of the 8th Lunar and Planetary Science Conference. Geochimica et Cosmochimica Acta Supplement 2253–2300.*

Steiger, R. H. & Jäger, E. (1977). Subcommission on Geochronology: convention on the use of deay constants in geo- and cosmochronology. *Earth and Planetary Science Letters* **36**, 359–362.

Török, K. & De Vivo, B. (1995). Fluid inclusions in upper mantle xenoliths from the Balaton Highland, Western Hungary. *Acta Vulcanologica* **7**, 277–284.

Trieloff, M. & Kunz, J. (2005). Isotope systematics of noble gases in the Earth's mantle: Possible sources of primordial isotopes and implications for mantle structure. *Physics of the Earth and Planetary Interiors* **148**, 13–38.

Trieloff, M., Reimold, W. U., Kunz, J., Boer, R. H. & Jessberger, E. K. (1994). ^{40}Ar–^{39}Ar thermochronology of pseudotachylite at the Ventersdorp Contact Reef, Witwatersrand Basin. *South African Journal of Geology* **97**, 365–384.

Trieloff, M., Weber, H. W., Kurat, G., Jessberger, E. K. & Janicke, J. (1997). Noble gases, their carrier phases, and argon chronology of upper mantle rocks from Zabargad Island, Red Sea. *Geochimica et Cosmochimica Acta* **61**, 5065–5088.

Trieloff, M., Kunz, J., Clague, D. A., Harrison, D. & Allègre, C. J. (2000). The nature of pristine noble gases in mantle plumes. *Science* **288**, 1036–1038.

Trieloff, M., Falter, M. & Jessberger, E. K. (2003). The distribution of mantle and atmospheric argon in oceanic basalt glasses. *Geochimica et Cosmochimica Acta* **67**, 1229–1245.

Turner, G. (1971). Argon 40–argon 39 dating: the optimization of irradiation parameters. *Earth and Planetary Science Letters* **10**, 227–234.

Turner, G., Burgess, R. & Bannon, M. (1990). Volatile-rich mantle fluids inferred from inclusions in diamond and mantle xenoliths. *Nature* **344**, 653–655.

Turner, G., Burnard, P., Ford, J. L., Gilmour, J. D., Lyon, I. C. & Stuart, F. M. (1993). Tracing fluid sources and interactions. *Philosophical Transactions of the Royal Society of London, Series A* **344**, 127–140.

Ukstins, I. A., Renne, P. R., Wolfenden, E., Baker, J., Ayalew, D. & Menzies, M. (2002). Matching conjugate volcanic rifted margins: ^{40}Ar/^{39}Ar chrono-stratigraphy of pre- and syn-rift bimodal flood volcanism in Ethiopia and Yemen. *Earth and Planetary Science Letters* **198**, 289–306.

Webb, S. A. C. & Wood, B. J. (1986). Spinel–pyroxene–garnet relationships and their dependence on Cr/Al ratio. *Contributions to Mineralogy and Petrology* **92**, 471–480.

Witt-Eickschen, G., Klemd, R. & Seck, H. A. (2003). Density contrast of fluid inclusions associated with melt (glass) from two distinct suites of mantle peridotites from the West Eifel, Germany: Implications for melt origin. *European Journal of Mineralogy* **15**, 95–102.